HIGH-PRECISION SR AND ND ISOTOPE MEASUREMENTS USING A DYNAMIC ZOOM LENS-EQUIPPED THERMAL IONISATION MASS SPECTROMETER

Tu-Han Luu, Pamela Gutiérrez, Edward C Inglis, Catherine Chauvel, Daniel J. Roberts

To cite this version:

Tu-Han Luu, Pamela Gutiérrez, Edward C Inglis, Catherine Chauvel, Daniel J. Roberts. HIGH-PRECISION SR AND ND ISOTOPE MEASUREMENTS USING A DYNAMIC ZOOM LENS-EQUIPPED THERMAL IONISATION MASS SPECTROMETER. Chemical Geology, 2022, 10.1016/j.chemgeo.2022.121078 . hal-03761496

HAL Id: hal-03761496
https://hal.science/hal-03761496v1

Submitted on 26 Aug 2022

HIGH-PRECISION SR AND ND ISOTOPE MEASUREMENTS USING A DYNAMIC ZOOM LENS-EQUIPPED THERMAL IONISATION MASS SPECTROMETER

Tu-Han Luu*[a], Pamela Gutiérrez[a], Edward C. Inglis[a,+], Daniel Roberts[b], Catherine Chauvel[a]

[a] Université Paris Cité, Institut de physique du globe de Paris, CNRS, F-75005 Paris, France
[b] Nu Instruments Ltd, Unit 74, Clywedog Road South, Wrexham Industrial Estate, LL13 9XS, United Kingdom

* Corresponding author: tluu@ipgp.fr
[+] Present address: School of Earth and Environmental Sciences, Cardiff University, Main Building, Park Place, Cardiff CF10 3AT, United Kingdom

Keywords

Nu TIMS, high precision Sr isotopic measurements, high precision Nd isotopic measurements

Significant statement

High precision Sr and Nd isotopic measurements are of key importance in the field of Earth Sciences because they are powerful tools to trace sources of materials and to date them. Here, we report the first high-precision data for ^{87}Sr/^{86}Sr and ^{143}Nd/^{144}Nd (external error of 5-6 ppm for Sr and 4-5 ppm for Nd) measured using a Nu Instruments TIMS. Such precisions will open new opportunities in fields such as geochemistry, geochronology, cosmochemistry, archaeology or forensics.

Abstract

Techniques for the determination of radiogenic strontium (^{87}Sr/^{86}Sr) and neodymium (^{143}Nd/^{144}Nd) isotope ratios by Thermal Ionisation Mass Spectrometry (TIMS) are presented in this study. We have developed a 5 lines acquisition routine for both elements, taking advantage of the 16 Faraday cups available on the Nu Instruments TIMS in conjunction with an efficient zoom lens system. This allows increased flexibility regarding the number of lines in a multidynamic acquisition routine whilst maintaining optimal peak alignment and peak shape for every measurement line despite the fact that the detectors are not movable. The long-term reproducibility obtained for our Sr (NBS 987) and Nd (Rennes-Ames) standard solutions gives a $(^{87}\text{Sr}/^{86}\text{Sr})_{\text{multidyn}}$ of 0.7102467 ± 0.0000043 (6.0 ppm, 2 s.d., n = 38) and a $(^{143}\text{Nd}/^{144}\text{Nd})_{\text{multidyn}}$ of 0.5119537 ± 0.0000022 (4.2 ppm, 2 s.d., n = 31), respectively. We also report $(^{87}\text{Sr}/^{86}\text{Sr})_{\text{multidyn}}$ and $(^{143}\text{Nd}/^{144}\text{Nd})_{\text{multidyn}}$ for a set of terrestrial rock standards (including 5 basalts (BCR-2, BHVO-2, BIR-1, Be-N and BR-24), one rhyolite (RGM-1) and one andesite (AGV-2)) with the same, or greater, level of precision as for the pure standards solutions. This level of precision is 2 to 3 times better than the literature data for Sr isotope ratios, and comparable to the latest high precision data reported for Nd isotope ratios. This is the first paper reporting such high precisions for radiogenic Sr and Nd data generated using a TIMS from Nu Instruments.

1. Introduction

Isotope geochemistry has been widely used to probe the evolution and heterogeneity of the terrestrial mantle (e.g., White 2015). Among the different tools available, radiogenic isotopes are of particular interest because (i) they are not directly fractionated by magmatic processes and thus are good source tracers, and (ii) they give information about the timing of processes *via* their parent-to-daughter decay ratios being time-integrated over the entire history of the Earth. A large number of isotope systems are available, but the most extensively used are the incompatible lithophile element systems: ^{87}Rb-^{87}Sr (half-life of 49.23 Ga), ^{147}Sm-^{143}Nd (half-life of 106 Ga), ^{176}Lu-^{176}Hf (half-life of 3.86 Ga), ^{138}La-^{138}Ce (half-life of 292.5 Ga), ^{238}U-^{206}Pb (half-life of 4.47 Ga), ^{235}U-^{207}Pb (half-life of 0.71 Ga), ^{232}Th-^{208}Pb (half-life of 14.05 Ga).

The ^{87}Rb-^{87}Sr and ^{147}Sm-^{143}Nd systems were the first used. A major advantage of these systems is that Rb is more incompatible than Sr while Sm is less incompatible than Nd during partial melting of the mantle. This results in a crust enriched in incompatible elements (high Rb/Sr and low Sm/Nd) and an upper mantle depleted in incompatible elements (low Rb/Sr and high Sm/Nd) after melt extraction. Pioneering work in the 1970s defined the ^{87}Sr/^{86}Sr and ^{143}Nd/^{144}Nd mantle array (De Paolo and Wasserburg, 1979), and since then traditional radiogenic (Sr-Nd-Pb) isotope compositions measured in oceanic island basalts (OIBs) around the world have refined the original mantle array to 5 end-member mantle components: DMM (for depleted MORB mantle), HIMU (corresponding to a reservoir with high ^{238}U/^{204}Pb and often associated with recycling of oceanic crust; Chauvel et al. 1992), EM1 and EM2 (for enriched mantle 1 and 2, which are reservoirs characterized by variable Rb/Sr and low Sm/Nd) and PREMA (for prevalent mantle) also called FOZO or C. Despite this, the exact number of end-member compositions and their nature are still highly debated. Indeed, establishing subtle differences depends on improved precision and accuracy of isotopic measurements.

Improvement in analytical techniques over the last years has led to better precisions for isotope measurements: differences of a few parts per million (ppm) can now be detected compared to precisions of the order of tens or hundreds of ppm in the late 1970s. This has allowed the definition of for example distinct parallel trends between EM1 and EM2 mantle end-members in the Ce-Nd isotope space or in the Hf-Nd isotope space (e.g., Doucelance et al. 2021; Béguelin et al. 2021), leading to a better constraint on the nature and the age of the recycled material responsible for the extended mantle heterogeneity. Another example of the utility of high precision measurements for radiogenic isotope systems comes from Abouchami et al. (2005) who used high precision Pb isotope data to report, for the first time, different trends between the two chains of Hawaiian volcanoes Loa and Kea, with only very little compositional overlap in their Pb isotope features. This has allowed to better constrain the structure and geometry of the plumes ascending to the surface. Similar fine structures could be found in the Sr-Nd isotopic space with the improvement in precision of Sr and Nd isotope data as reported in our study. Aside from mantle geochemistry, the improvements in analytical protocol have greatly advanced the field of geochronology. For example, the latest high-precision Sm-Nd geochronology data allow for the resolution of ages to a precision of ± 1.0 Ma on very small samples (1-10 ng of Nd; e.g., Starr et al., 2020).

In this paper, we demonstrate that the latest generation of thermal ionisation mass spectrometers (TIMS) from Nu Instruments allows precisions of a few ppm to be reached, by taking advantage of the presence of a large number of detectors accompanied by an efficient zoom lens system. As mentioned above, this will have important implications in the field of mantle geochemistry, but not only. Indeed, the Sr and Nd systematics are also powerful tools in fields such as cosmochemistry, archaeology, ocean chemistry or paleoclimatic studies, to only cite a few. Improving the precision on measurements should help establishing small differences in sources or in temporal variations, or it could be a key tool to distinguish minor changes in geological and environmental processes.

2. Chemical procedures

a. Sample digestion

Complete digestion of between 50 mg and 100 mg of rock powder was accomplished using a 3:1 mixture of 28N HF and 16N HNO_3 acids on a hotplate at ~ 120°C for at least two days. The samples were then dried down and redissolved two times with 5 ml of 6N HCl followed by 5ml of 2N HCl to decompose fluorides. The set of rock standards analysed in the course of this study comprises 5 basalts (BCR-2, BHVO-2, BIR-1, Be-N and BR-24), one rhyolite (RGM-1) and one andesite (AGV-2) to encompass a wide range of geological matrices.

b. Separation of strontium and neodymium

The Sr and Nd chemical separations were achieved in a two-step chromatographic procedure adapted from the one published in Chauvel et al. (2011). The first step, common to both elements, corresponds to a cation-exchange chromatography in HCl on a BioRad PolyPrep column filled with 2 ml of AG50W-X8 resin (200-400 mesh). This step allows the removal of major elements, while collecting the Sr fraction in 3.5N HCl and the LREE fraction in 6N HCl. From there, the Sr fraction was further purified using a small (~ 3 mm diameter) homemade shrink fit Teflon column filled with ~ 0.4 mL of Sr-spec resin (50-100 µm). Rubidium, and its interfering ^{87}Rb isotope, was removed using 3N HNO_3 and Sr was collected in ultrapure Milli-Q® water (18.2 MΩ.cm). On the other hand, the LREE fraction was further purified using a plastic column (~ 7 mm diameter) filled with ~ 1 mL of Ln-spec resin (50-100 µm). During this step, the Nd fraction is collected in 0.25N HCl, allowing to separate it from Sm, the main interfering species when measuring ^{143}Nd/^{144}Nd. Our chemical procedures give a total procedural blank of ~ 100 pg for Sr and ~ 25 pg for Nd.

Following the Sr and Nd chemical separations, we systematically analysed an aliquot of 5% of each processed sample on an Agilent 8900 triple quadrupole ICP-MS at the Institut de Physique du Globe de Paris. This allows for the determination of the Sr and Nd recoveries, but also to ensure that no residual trace of Rb and Sm is present in the Sr and Nd fractions that will be loaded on filaments. Strontium and Nd recoveries were > 75% and > 85% respectively, giving on average more than 20 µg Sr and more than 1.5 µg Nd subsequently available for analysis, with typically $Rb/Sr < 1\times10^{-5}$ and $Sm/Nd < 6\times10^{-5}$, for all the rock standards.

3. Strontium and neodymium isotope measurements by Nu TIMS

a. *Generalities*

Strontium and neodymium isotopes are generally measured in static mode (on both TIMS and MC-ICPMS), with all the ion beams acquired simultaneously. This configuration is easier to set up on a mass spectrometer, does not necessitate a large number of detectors, and provide isotopic results precise enough when looking at variability between samples of the order of tens of ppm of more. However, when higher precision data is required, isotope measurements in a dynamic mode allow to better compensate for the relative deterioration of the Faraday detectors and their change in efficiency with time, and thus return more accurate isotopic results (e.g., Avanzinelli et al. 2005, Henshall et al. 2018, Fukai et al. 2017).

A Nu TIMS was installed at the Institut de Physique du Globe de Paris early 2020 (Serial No. 010) to perform high-precision Sr and Nd isotope measurements, in addition to other isotope systems such as Ca and W isotopes for instance. The instrument is equipped with 16 fixed Faraday detectors, that can be dynamically connected to amplifiers with different feedback resistors (10^{10}, 10^{11}, 10^{12} and 10^{13} Ω). The fixed Faraday detectors system is compensated by the presence of a zoom-lens system located between the magnet and the detector array (Fig. 1a). This zoom-lens system is made of two lenses: quad 1 primarily focuses the individual beams, while quad 2 controls the dispersion of the beams relative to each other. The large number of detectors, in conjunction with an efficient zoom lens system, allows significant flexibility regarding the number of lines in a multidynamic acquisition routine whilst maintaining optimal peak alignment and peak shape for every measurement line despite the fact that the detectors are not movable. In practice, the natural dispersion of the Nu TIMS is such that the Re isotopes will align in adjacent collectors without the need for any quadratic field being applied to the zoom lens system. As we go lower in mass (as for Nd and Sr isotopes compared to Re), the distance between the isotopes increases (Fig. 1a-1), because lighter elements will be separated more as they pass through the magnetic sector. Applying the correct set of voltages to the zoom lens system (quad 1 and quad 2 values in Table 1, referring to the electrostatic field applied across each lens stack) will create a continuous electrostatic field which then effectively acts to demagnify the mass separation at the detectors by deflecting the isotopes increasingly when moving farther away from the central point of the lens stack (Fig. 1a-2 and 1a-3). This allows for the alignment of the isotopes into the adjacent collectors whilst maintaining good peak shapes (Fig. 1b). Optimal alignment is now achieved electrostatically and not mechanically, allowing a robust and reproducible alignment within milliseconds and insuring robust conditions for multidynamic measurements. The benefit of a multidynamic acquisition routine is a better correction for cup efficiencies compared to static measurements, a better constraint on the oxide corrections when running in negative mode (for W isotopes for instance) and a better external reproducibility. Note that for Sr and Nd isotope analyses, all the Faraday cups used were connected to amplifiers with a 10^{11} Ω feedback resistor, and a 30 min gain calibration was performed every morning.

Strontium isotopic measurements were performed using roughly 300 ng of Sr loaded on previously outgassed zone-refined Re single filaments. About 0.7 µl of TaF_5 activator and 1 µl of sample in 0.5N HNO_3 were loaded onto the filament, in between two Parafilm strips separated by ~ 3 mm, at ~ 0.75 A. The role of the Parafilm strips was to prevent the sample and the activator spreading on the filament during the loading, so that a small spot could be obtained. The activator and the sample were left to dry down between each step. The Parafilm strips were then burnt off at ~ 1.6 A and the filament glowed briefly to dull red at ~ 2.0 A. Rubidium interferences were monitored on the TIMS using ^{85}Rb, but even in the case of residual rubidium, it was burnt off from the filament before the strontium was properly emitted. The sample filament was slowly heated until a stable $^{88}Sr^+$ beam of ~ 12-13 V was obtained and typically measured for 6-7 h (corresponding to ~ 200 cycles, with a total acquisition time of 80 s per cycle). The run length was variable and depended on when the sample was consumed. This translated into 'raw' $^{86}Sr/^{88}Sr$ typically close to 0.1204 at the start of an analysis and lower than 0.1185 (and sometimes even down to 0.1180) when the analysis stopped. Baselines were measured for 3 min every 20 cycles and peaks were recentred every 40 cycles.

Strontium isotopes were measured using a 5 lines acquisition routine (Table 1a). The $^{87}Sr/^{86}Sr$ and $^{84}Sr/^{86}Sr$ acquired in each line were corrected for instrumental mass fractionation with the exponential law using the $^{86}Sr/^{88}Sr$ acquired in the same line and assuming $(^{86}Sr/^{88}Sr)_{ref}$ = 0.1194. A multi-static $^{87}Sr/^{86}Sr$ (hereafter $(^{87}Sr/^{86}Sr)_{multistat}$) and a multi-static $^{84}Sr/^{86}Sr$ (hereafter $(^{84}Sr/^{86}Sr)_{multistat}$) can then be obtained by averaging the 5 static $^{87}Sr/^{86}Sr$ acquired in the 5 lines and the 4 static $^{84}Sr/^{86}Sr$ acquired in the first 4 lines, respectively. A dynamic $^{87}Sr/^{86}Sr$ is obtained by combining the measurements from two different magnetic field positions (e.g., lines 1 -2, Table 1a), following:

$$\left(\frac{^{87}Sr}{^{86}Sr}\right)_{1-2} = \sqrt{\left(\frac{^{87}Sr_{H9}}{^{86}Sr_{H7}}\right)_{1} \times \left(\frac{^{87}Sr_{H7}}{^{88}Sr_{H9}}\right)_{2} \times \left(\frac{^{88}Sr}{^{86}Sr}\right)_{ref}} \tag{1}$$

We can note that a correction for time-drift is applied for dynamic ratios (Garçon et al. 2018), and although the drift correction code may not be identical to Garçon et al. (2018), a similar effect can be seen. This time drift correction is utilized to minimize effects associated with a growing or changing signal emission between magnet positions. It does so by adding an extra measurement line at the start of each block and comparing this measurement to the following for a correction back to a set time and intensity. A multi-dynamic $^{87}Sr/^{86}Sr$ (hereafter $(^{87}Sr/^{86}Sr)_{multidyn}$) can then be obtained by averaging the 4 dynamic $^{87}Sr/^{86}Sr$. As mentioned earlier, we favoured dynamic measurements because they allow for the effective correction of potential differences in cup efficiencies and amplifier gains between Faraday detectors. Using the analytical conditions described above (very long and high intensity analysis), we obtained internal precision for an individual Sr analysis typically better than 2 x 10^{-6} (2 se) on $(^{87}Sr/^{86}Sr)_{multidyn}$ (Fig.2). In comparison, a 2 hours analysis (corresponding to more 'conventional' Sr isotope studies but with much higher intensities) gives an internal precision typically around 2.5 x 10^{-6} (2 se) on $(^{87}Sr/^{86}Sr)_{multidyn}$ (Fig.2). Finally, assuming that our analyses are made with a ^{88}Sr signal 4 to 10 times higher than 'conventional' Sr isotopes studies, we can estimate the internal precisions that would be obtained for 2 hours runs at low signal (1-3V on ^{88}Sr); these would be ~ 5-8 x 10^{-6} (Fig. 2). Such values are comparable to the internal precisions obtained in similar conditions and using other TIMS (e.g., Carpentier et al. 2014) or another Nu TIMS (e.g., Fourny et al. 2016, 2019).

Neodymium isotopic measurements were performed using between 600 ng and 800 ng of Nd loaded on previously outgassed zone-refined Re double filaments. About 1 µl of sample in 0.5N HNO_3 was loaded onto the sample filament, in between two Parafilm strips at ~ 0.75 A. Once dried, roughly 0.5 µl of 1N H_3PO_4 activator was loaded on top of the sample at ~ 1.2 A. Then, once the activator was dried and similarly to Sr, the Parafilm strips were burnt off at ~ 1.6 A and the filament glowed briefly to dull red at ~ 2.0 A. After having heated the ioniser filament to a temperature of ~ 1900°C in the source chamber, the sample filament was slowly heated until a stable $^{142}Nd^+$ beam of ~ 6-8 V was obtained and typically measured for 7-8 h (corresponding to ~ 300 cycles, with a total acquisition time of 50 s per cycle). Unlike for Sr analyses, we did not systematically run until the Nd was totally consumed. However, if the sample was getting exhausted by the end of an analysis, it translated into 'raw' $^{146}Nd/^{144}Nd$ typically starting at 0.7200 to finish at 0.7250 when the analysis was stopped. Baselines were measured for 3 min every 20 cycles, and peaks were recentred every 60 cycles.

Similarly to the Sr method, Nd isotopes were measured using a 5 lines acquisition routine (Table 1b). The method and the equations described in this paper for Nd isotope measurements on the Nu TIMS are adapted from Thirlwall (1991) and Garçon et al. (2018). The $^{143}Nd/^{144}Nd$, $^{145}Nd/^{144}Nd$, $^{148}Nd/^{144}Nd$ and $^{150}Nd/^{144}Nd$ acquired in each line were corrected for instrumental mass fractionation with the exponential law using the $^{146}Nd/^{144}Nd$ acquired in the same line and assuming $(^{146}Nd/^{144}Nd)_{ref} = 0.7219$. A multi-static $^{i}Nd/^{144}Nd$ (hereafter $(^{i}Nd/^{144}Nd)_{multistat}$, with i = 143, 145, 148 or 150) can then be obtained by averaging the 5 static $^{i}Nd/^{144}Nd$ acquired in the 5 lines. Dynamic $^{143}Nd/^{144}Nd$ and $^{145}Nd/^{144}Nd$ are obtained by combining the measurements from three different magnetic field positions (i.e. lines 1-2-3, 2-3-4 or 3-4-5, Table 1b), following for instance:

$$\left(\frac{^{143}Nd}{^{144}Nd}\right)_{1-2-3} = \sqrt{\left(\frac{^{143}Nd_{H1}}{^{144}Nd_{H2}}\right)_{3} \times \left(\frac{^{143}Nd_{Ax}}{^{144}Nd_{H1}}\right)_{2} \times \left(\frac{m_{143}}{m_{144}}\right)^{2F_1}} \quad (2)$$

$$\text{With } F_1 = \frac{\ln\left(\frac{\left(\frac{^{146}Nd}{^{144}Nd}\right)_{ref}}{\left(\frac{^{146}Nd_{H2}}{^{144}Nd_{Ax}}\right)_{1}}\right)}{\ln\left(\frac{m_{146}}{m_{144}}\right)} \quad (3)$$

Dynamic $^{148}Nd/^{144}Nd$ and $^{150}Nd/^{144}Nd$ are obtained by combining the measurements from two different magnetic field positions (i.e. lines 1-3, 2-4 or 3-5, Table 1b), following for instance:

$$\left(\frac{^{148}Nd}{^{144}Nd}\right)_{1-3} = \left(\frac{^{148}Nd_{H4}}{^{146}Nd_{H2}}\right)_{1} \times \left(\frac{^{146}Nd}{^{144}Nd}\right)_{ref} \times \left(\frac{m_{148}}{m_{146}}\right)^{F_3} \quad (4)$$

$$\text{With } F_3 = \frac{\ln\left(\frac{\left(\frac{^{146}Nd}{^{144}Nd}\right)_{ref}}{\left(\frac{^{146}Nd_{H4}}{^{144}Nd_{H2}}\right)_{3}}\right)}{\ln\left(\frac{m_{146}}{m_{144}}\right)} \quad (5)$$

As in the Sr procedure, a correction for time-drift is applied for dynamic ratios. A multi-dynamic $^{i}Nd/^{144}Nd$ (hereafter $(^{i}Nd/^{144}Nd)_{multidyn}$) can then be obtained by averaging the 3 dynamic $^{i}Nd/^{144}Nd$. Using the analytical conditions described above (very long and high intensity analysis), we obtain internal precision for an individual Nd analysis typically better than 1 x 10^{-6} (2 se) on $(^{143}Nd/^{144}Nd)_{multidyn}$. We do not report values for $^{142}Nd/^{144}Nd$ in this paper because the chromatographic procedure used in the course of this study was not designed to remove Pr and Ce from Nd (Table 2b).

b. *Reproducibility of pure standard solutions*

We obtain $(^{87}Sr/^{86}Sr)_{multidyn}$ = 0.7102467 ± 0.0000043 (6.0 ppm, 2 s.d., n = 38) for NBS 987 (Fig. 3) and $(^{143}Nd/^{144}Nd)_{multidyn}$ = 0.5119537 ± 0.0000022 (4.2 ppm, 2 s.d., n = 31) for Rennes-Ames (Fig. 4). We can note here that if we consider only the sub data corresponding to the first 60 cycles (~ 2 hours) of each NBS 987 analysis, we obtain similar values, i.e. $(^{87}Sr/^{86}Sr)_{multidyn}$ = 0.7102456 ± 0.0000044 (6.2 ppm, 2 s.d., n = 38). These data are consistent with the data reported in the literature, however the external precisions reported here on pure standard solutions are two to three times better than the most precise published data for $^{87}Sr/^{86}Sr$, and comparable to the most precise literature data for $^{143}Nd/^{144}Nd$ (Table 3 and Fig. 3a and 4a).

Our measurement of JNdi-1 gives $(^{143}Nd/^{144}Nd)_{multidyn}$ = 0.5120941 ± 0.0000022 (4.4 ppm, 2 s.d., n = 9), which is slightly lower than the reference value of 0.512115 ± 0.000007 reported in Tanaka et al. (2000). However, our $(^{143}Nd/^{144}Nd)_{multidyn}$ is in agreement with the high-precision data of 0.512099 ± 0.000005 (9.2 ppm, 2 s.d., n = 54) reported in Garçon et al. (2018). It is also very close to the latest high-precision data reported by Pin and Gannoun (2019 a,b) of 0.512101 ± 0.000003 (5.9 ppm, 2 s.d., n = 12) and 0.512104 ± 0.000003 (5.9 ppm, 2 s.d., n = 15). We note that despite plotting within error of each other, the two values reported by Pin and Gannoun indicate that small variations can occur for analyses run on the same instrument in the same laboratory, even in the course of high precision isotope work.

Also, as seen in Figure 3b, there is no resolvable difference between $(^{87}Sr/^{86}Sr)_{multidyn}$ and $(^{87}Sr/^{86}Sr)_{multistat}$, which is expected when the drift in the mass bias is corrected properly and the Faraday cups show little evidence for deterioration (the detectors have been used for less than a year in the course of this study). Similarly to $^{87}Sr/^{86}Sr$, there seems to be no significant offset between $(^{143}Nd/^{144}Nd)_{multidyn}$ and $(^{143}Nd/^{144}Nd)_{multistat}$, the difference between the two ratios being on average ~ 2 ppm , i.e. within error (Fig. 4b). It is also important to note that for the Nd systematics, the multidynamic method yields more reproducible data than the multistatic method, translating into a smaller error on the mean ratio (± 0.0000022 *versus* ± 0.0000040 on the $^{143}Nd/^{144}Nd$, 2 s.d., n = 31). For the Sr systematics, both methods seem to give comparable reproducibility at the moment (± 0.0000043 *versus* ± 0.0000041 on the $^{87}Sr/^{86}Sr$, 2 s.d., n=38). One thing worth to note here is that, as shown in Figure 4b, the $^{143}Nd/^{144}Nd$ seems to decrease with time (for both $(^{143}Nd/^{144}Nd)_{multidyn}$ and $(^{143}Nd/^{144}Nd)_{multistat}$). The origin of this drift is not clear to us yet, but we believe it could be several things, from how the beam behaves (growing or dying), how it fractionates (i.e. reverse fractionation occurring; e.g., Garçon et al. 2018) to the gain or the bucket efficiency. Thus, if we can see a 4 ppm change between running the analysis using a standard or reverse cup configuration (see below), maybe the same could be seen between a growing and dying signal. Alternatively, a good indication of bucket efficiency would be to monitor how the ^{143}Nd/^{144}Nd static ratios behave individually when the gain is stable over a time period. However, we could not see one (^{143}Nd/^{144}Nd)$_{\mathrm{stat}}$ being systematically and significantly lower than the others. Overall, it is difficult to say what causes this change given it is a very small change.

Furthermore, we have compared two reverse methods (Table 1b and 1c) for Nd isotope measurements on the pure standard solution Rennes-Ames and have noticed the (^{143}Nd/^{144}Nd)$_{\mathrm{multidyn}}$ obtained with each method were within errors of each other. Thus, in February 2021, we obtained a (^{143}Nd/^{144}Nd)$_{\mathrm{multidyn}}$ of 0.5119535 ± 0.0000013 (2.5 ppm, 2 s.d., n = 7) with the cup configuration reported in table 1b, which is within error of (^{143}Nd/^{144}Nd)$_{\mathrm{multidyn}}$ = 0.5119514 ± 0.0000018 (3.5 ppm, 2 s.d., n = 5) obtained with the reverse method reported in table 1c. The relative difference between those two values is of ~ 4 ppm. Similarly, we obtained the same relative difference of ~ 4 ppm for (^{143}Nd/^{144}Nd)$_{\mathrm{multidyn}}$ between the two Nd reverse methods in June 2021, with the cup configuration reported in table 1b giving 0.5119500 ± 0.0000004 and the set-up reported in Table 1c giving 0.5119481 ± 0.0000007. Overall, although the method reported in Table 1b seems to give a slightly higher (^{143}Nd/^{144}Nd)$_{\mathrm{multidyn}}$, this is not significant compared to the external reproducibility (2 s.d.) of 4-5 ppm reported in this study for (^{143}Nd/^{144}Nd)$_{\mathrm{multidyn}}$. The cup configuration reported in Table 1b was the one finally used during this study.

Finally, the data obtained in this study for stable isotopes, i.e. ^{84}Sr/^{86}Sr = 0.0564902 ± 0.0000018 (31.9 ppm, 2 s.d., n = 38) for NBS 987, and ^{145}Nd/^{144}Nd = 0.3484004 ± 0.0000013 (3.7 ppm, 2 s.d., n = 31), ^{148}Nd/^{144}Nd = 0.2415798 ± 0.0000019 (8.0 ppm, 2 s.d., n = 31) and ^{150}Nd/^{144}Nd = 0.2364508 ± 0.0000056 (23.5 ppm, 2 s.d., n = 31) for Rennes-Ames, are consistent with previous studies (Table 3). The precisions reported here on those ratios are comparable to the latest high-precision isotope data reported in Burkhardt et al. (2019) for the Sr standard solution NBS 987 and Pin and Gannoun (2019) for the Nd standard solution Rennes-Ames (Fig. 5).

c. Precision

In this section, we compare the actual errors of our analyses on the Nu TIMS with the theoretical uncertainties expected from Johnson-Nyquist noise and counting statistics, these processes being considered as the two main contributors to the observed internal uncertainty for a given analysis. The reader is referred to the supplementary section of Luu et al. (2019) for more details about the theoretical uncertainty model and the calculations, but the important details are summarized below.

Johnson-Nyquist noise ($\sigma_{\mathrm{Johnson}}$), the phenomenon of thermally-generated voltage noise in the feedback resistor, has a standard deviation given by $\sigma_{Johnson} = \sqrt{\frac{4RkT}{t}}$, where R is the feedback resistor of the amplifier connected to the Faraday cup (here 10^{11} Ω for all cups measuring Sr and Nd isotopes), k is the Boltzmann constant (= 1.38×10^{-23} J/K), T is the amplifier housing temperature (= 307 K) and t is the total integration time (= integration time per static measurement × total number of cycles). Note that we include this noise in our uncertainty model for completeness, but it is insignificant compared to the shot noise. Counting statistics (σ_{counting}), or shot noise, describes the statistics of the arrival of ions at the detector as a Poisson distribution. It is given by $\sigma_{counting} = \sqrt{\frac{V_m R e}{t}}$, where V_m is the mean amplifier output voltage over the total integration time t, and e is the elementary charge (= 1.60×10^{-19} C). Combining these errors by adding in quadrature the total absolute error on each isotope gives $\sigma_{abs}^{x} = \sqrt{\sigma_{Johnson}^{2} + \sigma_{counting}^{2}}$, and the total relative error can be written as $\sigma_{rel}^{x} = \frac{\sigma_{abs}^{x}}{V_m^x}$, with x = 86, 87 or 88 for Sr isotopes for instance. From there, the 2 s.e. relative error on the $(^{87}\text{Sr}/^{86}\text{Sr})_{\text{multidyn}}$ is derived by the quintuple jump type error propagation calculation as: $2se_{rel}^{multidyn} = 2 \times \frac{1}{2n}\sqrt{n \times (\sigma_{rel}^{x})^2 + n \times (\sigma_{rel}^{z})^2 + (4n-2) \times \left(\sigma_{rel}^{y}\right)^2}$, where n correspond to the number of static measurements – 1 (so n = 4 in our case). Finally, the 2 s.e. absolute error on the $(^{87}\text{Sr}/^{86}\text{Sr})_{\text{multidyn}}$ is calculated as: $2se_{abs}^{multidyn} = 2se_{rel}^{multidyn} \times \frac{A_{87}}{A_{86}}$, where A_{87} and A_{86} correspond to the relative abundances of ^{87}Sr (7.00%) and ^{86}Sr (9.86%) isotopes, respectively. The reader is referred to the supplementary information of this paper for more details about these equations and the error propagation calculations.

The results of that model are plotted in Figure 6, for the case of Sr systematics. We chose to plot the typical internal precisions (2 s.e.) for $(^{87}\text{Sr}/^{86}\text{Sr})_{\text{multidyn}}$ against 1/sqrt(number of ions detected) because this latter parameter reflects the total integration time, while accounting for the different average total intensities of the dataset. On figure 6a, we can clearly see that the data fall below the model, for both the geostandards and the pure standard solution NBS 987. This is unexpected and may not look correct at first glance. However, we used a Monte Carlo simulation for the quintuple-jump uncertainty on the ratio and it agrees well with the error propagation model described above, so we are confident that the discrepancy between the actual and the theoretical errors is not due to a mistake in the algebra of propagating the errors.

We then investigated the effect of the time-drift correction. As mentioned earlier, a correction for time-drift is applied for dynamic ratios. This is because the use of a time-drift correction in a dynamic routine helps reducing possible fractionation changes between measurement lines, which could cause a bias on the final ratio as suggested in Garçon et al. (2018) and observed by Roth et al. (2014). We note that although the drift correction code may not be identical to Garçon et al. (2018), a similar effect can be seen. If the time-drift correction is ignored, it appears that the data are now consistent with the model (Fig. 6b): the typical uncertainties reported in Table 3 for both pure standard solution NBS987 and terrestrial rock standards are now very close to the modelled errors, showing that (i) there is no effect of the matrix on the precision of an analysis, and that (ii) the Nu TIMS is performing at the best of its capabilities. We can note that the $(^{87}\text{Sr}/^{86}\text{Sr})_{\text{multidyn}}$ with and without time drift correction are differing by less than 4 ppm (Table 4), which is not significant compared to the 6 ppm external reproducibility we report. Thus, all the data reported in this paper have been processed using a time drift correction.

4. Results for terrestrial rock standards

The $(^{87}Sr/^{86}Sr)_{multidyn}$ and $(^{143}Nd/^{144}Nd)_{multidyn}$ obtained for rock standards in this study are reported in Table 3. All the results obtained by our method are in agreement with published data (Fig. 7 and 8). For instance, we obtained $(^{87}Sr/^{86}Sr)_{multidyn} = 0.7034750 \pm 0.0000023$ (3.3 ppm, 2 s.d., n = 4) and $(^{143}Nd/^{144}Nd)_{multidyn} = 0.5129662 \pm 0.0000025$ (4.8 ppm, 2 s.d., n = 4) for BHVO-2, and $(^{87}Sr/^{86}Sr)_{multidyn} = 0.7039814 \pm 0.0000059$ (8.3 ppm, 2 s.d., n = 4) and $(^{143}Nd/^{144}Nd)_{multidyn} = 0.5127702 \pm 0.0000033$ (6.4 ppm, 2 s.d., n = 3) for AGV-2. We should note that the variability in $^{143}Nd/^{144}Nd$ for JNdi-1 between different studies (see section 3.b) has to be taken into account when comparing the $^{143}Nd/^{144}Nd$ in the literature for terrestrial standards. The important thing to note here is that, for both systems, the precisions reported in this study are much better than most previous studies (Fig. 7 and 8), with an external reproducibility of typically 5-6 ppm (2 s.d.) for $^{87}Sr/^{86}Sr$ and 4-5 ppm (2 s.d.) for $^{143}Nd/^{144}Nd$. We can also note that, although our chemistry protocol does not remove ^{141}Pr nor ^{140}Ce (with typically $2 < {}^{141}Pr^+/{}^{146}Nd^+ < 4$ and ${}^{140}Ce^+/{}^{146}Nd^+ < 1$ for rock standards at the start of an analysis), this does not seem to affect the accuracy of the $^{143}Nd/^{144}Nd$.

5. Implications

The level of precision reached for Sr and Nd systematics in this study opens new perspectives in the field of Earth Sciences, but not only.

Indeed, the extent of the application of radiogenic isotopes is not restricted to Earth Sciences. In archaeology, $^{87}Sr/^{86}Sr$ and $^{143}Nd/^{144}Nd$ represent a powerful tool as source tracers. For instance, small differences in isotope ratios can be decisive in discriminating sources at the origin of raw materials that have been used for making prehistoric artefacts, and this information can be precious to understand patterns of migrations and/or interactions between prehistoric societies. However, few data have been produced with good precision (e.g., Weisler et al. 2016, Hermann et al. 2017) and thereby most studies have limited conclusions given the geochemical similarity of sources and some unclear geological complications regarding the source of Sr (e.g., Thomsen and Andreasen, 2019).

In cosmochemistry, small isotopic anomalies, commonly down to the ppm level, are present among solar system materials at a planetary scale, and so, being able to detect them provide important constraints on planetary bodies relationships and the dynamical evolution of the solar system. Considering Sr isotopes, the level of analytical precision of most studies (~ 8-10 ppm, 2 s.e.; e.g., Hans et al. 2013, Henshall et al. 2018) did not allow identification of mass-independent variations in $^{84}Sr/^{86}Sr$ between enstatite chondrites, ordinary chondrites, eucrites, Moon, Mars and the Earth; only carbonaceous chondrites showed small resolvable positive anomalies in ^{84}Sr, between 40 and 60 ppm relative to NBS 987 (e.g., Moynier et al. 2012). The latest study of bulk planetary materials by Burkhardt et al. (2019) has modified this picture, reporting ordinary and enstatite chondrites, as well as Moon, with small resolvable negative anomalies in ^{84}Sr, on the order of -10 to -20 ppm relative to NBS 987. This demonstrates that improving analytical precision is key to better resolve small isotopic variability, and thus why the level of precision reached for ^{84}Sr/^{86}Sr in this study (2 s.e. of ~ 5 ppm, Fig. 5a) is useful. The same reasoning could be true for other systematics, e.g. mass-independent variations in ^{40}Ca.

High precision data such as those reported in this study also opens new chronology perspectives. Even if most of the uncertainty on ages comes from the poor determination of the parent/daughter ratio, enhanced precision on the isotopic ratio translates into a smaller propagated uncertainty on the age determined from Rb-Sr or Sm-Nd isochrons (Fig. 9). We should be able to obtain Rb-Sr or Sm-Nd isochrons for much younger rocks, with greater resolution between previously indistinguishable suites. We should also be able to obtain isochrons for phases with lower Rb/Sr or Sm/Nd, for which the excesses in the decay products of ^{87}Rb and ^{143}Sm will be small but now detectable with our improved analytical precisions on ^{87}Sr/^{86}Sr and ^{143}Nd/^{144}Nd. For example, recently, Baxter et al. (2017) reported high-precision Sm-Nd dating of individual growth zones within single garnet crystals in eclogites and other metamorphic rocks, and highlighted multistage processes occurring in subduction.

In mantle geochemistry, small scale mantle heterogeneities, such as those discovered when Pb isotopes started being measured with high precision (e.g., Abouchami et al. 2005), might be discovered for volcanic rocks in both Sr and Nd isotopic spaces. Indeed, before the study by Abouchami et al. (2005), the two chains of Hawaiian volcanoes Loa and Kea were thought to have overlapping radiogenic isotope features (for Pb, Sr and Nd systematics). However, the high precision Pb isotope data reported for the first time in Abouchami et al. (2005) thanks to a Pb triple-spike technique have allowed to differentiate the Loa and Kea trends, with only a very little compositional overlap. Similar discoveries could be expected with the improvement in precision of Sr and Nd isotope data as reported in our study.

Finally, the preservation in the Earth's deep interior of early-formed material, either recycled from the surface reservoirs or residual from the early mantle differentiation, has recently been evidenced by the detection of small variability in ^{182}W (Mundl et al. 2017, Rizo et al. 2016) and ^{142}Nd (Peters et al. 2018), the decay products of the short-lived ^{182}Hf (half-life of 8.9 Myr) and ^{146}Sm (half-life of 103 Myr), respectively. The total range of variations among modern ocean island basalts does not exceed 15 ppm in ^{142}Nd/^{144}Nd and 25 ppm for ^{182}W/^{184}W. These small variabilities have become detectable thanks to the high analytical precisions recently reached with dynamic measurements on the TIMS, i.e. ± 4 ppm on ^{182}W/^{184}W (2 s.d.; Mundl et al. 2017) and ± 4.4 ppm on ^{142}Nd/^{144}Nd (2 s.d., in Peters et al. 2018). These recent discoveries are very exciting and we are currently developing analytical methods for high precision ^{182}W and ^{142}Nd isotope measurements on our Nu TIMS at IPGP, in order to expand the currently limited dataset available.

6. Conclusions

We report high-precision Sr and Nd isotope data, with an external reproducibility on the order of 5-6 ppm (2 s.d.) for ^{87}Sr/^{86}Sr and 4-5 ppm (2 s.d.) for ^{143}Nd/^{144}Nd. This is the first time such a level of precision is reported with a TIMS from Nu Instruments. Such precisions are of key importance in the field of Earth Sciences because Sr and Nd systematics are powerful tools to trace sources of materials and to date them, but they also open new opportunities in fields such as cosmochemistry, paleoclimatic studies, archaeology, tracing of food origin or forensics.

7. Acknowledgements

This work was supported by grant from European Research Council (ERC grant SHRED, Grant Agreement no. [833632] – Survival of Hadean REmnants in a Dynamic mantle). THL would like to thank Christopher Coath from the Bristol Isotope Group for his expertise regarding the statistics and error propagation section and acknowledge authorship of the derivation of the theoretical uncertainty provided in the supplementary information. We thank Tod Waight and an anonymous reviewer for their constructive reviews that allowed for a much-improved manuscript. We also thank Balz Kamber for editorial handling.

8. References

1. Abouchami, W., et al., 2005. Lead isotopes reveal bilateral asymmetry and vertical continuity in the Hawaiian mantle plume. Nature 434, 851–856.
2. Aciego, S.M., Bourdon, B., Lupker, M., Rickli, J., 2009. A new procedure for separating and measuring radiogenic isotopes (U, Th, Pa, Ra, Sr, Nd, Hf) in ice cores. Chem. Geol. 266, 194–204.
3. Ali, A. and Srinivasan, G., 2011. Precise thermal ionization mass spectrometric measurements of ^{142}Nd/^{144}Nd and ^{143}Nd/^{144}Nd isotopic ratios of Nd separated from geological standards by chromatographic methods. Int. J. Mass Spectrom. 299, 27–34.
4. Avanzinelli, R., et al., 2005. High precision Sr, Nd and Pb isotopic analyses using the new generation Thermal Ionisation Mass Spectrometer ThermoFinnigan Triton-Ti®. Per. Mineral. 74, 147–166.
5. Baxter, E.F., Caddick, M.J., Dragovic, B., 2017. Garnet: a rock forming mineral petrochronometer. Rev. Mineral. Geochem. 83, 469–533.
6. Béguelin, P., et al. 2021. Cerium isotope constraints on the nature of the Azores plume. Goldschmidt Abstracts.
7. Burkhardt, C., et al., 2019. Elemental and isotopic variability in solar system materials by mixing and processing of primordial disk reservoirs. Geochim. Cosmochim. Acta 261, 145–170.
8. Caro, G., Bourdon, B., Birck, J.-L., Moorbath, S., 2003. ^{146}Sm-^{142}Nd evidence from Isua metamorphosed sediments for early differentiation of the Earth's mantle. Nature 423, 428–432.
9. Caro, G., Bourdon, B., Birck, J.-L., Moorbath, S., 2006. High-precision ^{142}Nd/^{144}Nd measurements in terrestrial rocks: Constraints on the early differentiation of the Earth's mantle. Geochim. Cosmochim. Acta 70, 164–191.

10. Carpentier, M., Weis, D., Chauvel, C., 2014. Fractionation of Sr and Hf isotopes by mineral sorting in Cascadia Basin terrigenous sediments. Chem. Geol. 382, 67–82.
11. Chauvel, C., Hofmann, A.W., Vidal, P., 1992. HIMU-EM: the French Polynesian connection. Earth Planet. Sci. Lett. 110, 99–119.
12. Chauvel, C. and Blichert-Toft, J., 2001. A hafnium isotope and trace element perspective on melting of the depleted mantle. Earth Planet. Sci. Lett. 190, 137–151.
13. Chauvel, C., Bureau, S., Poggi, C., 2011. Comprehensive chemical and isotopic analyses of basalt and sediment reference materials. Geostand. Geoanalytical Res. 35, 125–143.
14. Chu, Z., Chen, F., Yang, Y., Guo, J., 2009. Precise determination of Sm, Nd concentrations and Nd isotopic compositions at the nanogram level in geological samples by thermal ionization mass spectrometry. J. Anal. Atom. Spectrom. 24, 1534–1544.
15. De Paolo, D.J. and Wasserburg, G.J., 1979. Petrogenetic mixing models and Nd-Sr isotopic patterns. Geochim. Cosmochim. Acta 43, 615–627.
16. Di, Y., Krestianinov, E., Zink, S., Amelin, Y., 2021. High-precision multidynamic Sr isotope analysis using thermal ionization mass spectrometer (TIMS) with correction of fractionation drift. Chem. Geol. 582, 120411.
17. Doucelance, R., et al., 2021. A Ce-Nd-Hf isotope perspective on the EMI-EMII end-member. Goldschmidt Abstracts.
18. Fourny, A., Weis, D., Scoates, J.S., 2016. Comprehensive Pb-Sr-Nd-Hf isotopic, trace element and mineralogical characterization of mafic to ultramafic rock reference materials. Geochem. Geophys. Geosyst. 17, 739–773.
19. Fourny, A., Weis, D., Scoates, J.S., 2019. Isotopic and trace element geochemistry of the Kiglapait intrusion, Labrador: Deciphering the mantle source, crustal contributions and processes preserved in mafic layered intrusions. J. Petrol. 60, 553–590.
20. Fukai, R., Yokoyama, T., Kagami, S., 2017. Evaluation of the long-term fluctuation in isotope ratios measured by TIMS with the static, dynamic, and multistatic methods: A case study for Nd isotope measurements. Int. J. Mass Spectrom. 414, 1–7.
21. Garçon, M., et al., 2018. Factors influencing the precision and accuracy of Nd isotope measurements by thermal ionization mass spectrometry. Chem. Geol. 476, 493–514.
22. Hans, U., Kleine, T., Bourdon, B., 2013. Rb-Sr chronology of volatile depletion in differentiated protoplanets: BABI, ADOR and ALL revisited. Earth Planet. Sci. Lett. 374, 204–214.
23. Henshall, T., Cook, D.L., Garçon, M., Schönbächler, M., 2018. High-precision strontium isotope analysis of geological samples by thermal ionization mass spectrometry. Chem. Geol. 482, 113–120.
24. Hermann, A., et al., 2017. Combined geochemical and geochronological analyses of stone artefacts provide unambiguous evidence of intra- and inter-island interactions in Polynesia. Journal of Archaeological Science: Report 13, 75–87.
25. Jweda, J., Bolge, L., Class, C., Goldstein, S.L., 2016. High precision Sr-Nd-Hf-Pb isotopic compositions of USGS reference material BCR-2. Geostand. Geoanalytical Res. 40, 101–115.
26. Klaver, M., et al., 2015. Temporal and spatial variations in provenance of Eastern Mediterranean Sea sediments: Implications for Aegean and Aeolian arc volcanism. Geochim. Cosmochim. Acta 153, 149–168.

27. Koornneef, J.M., et al., 2015. TIMS analysis of Sr and Nd isotopes in melt inclusions from Italian potassium-rich lavas using prototype 10^{13} Ω amplifiers. Chem. Geol. 397, 14–23.
28. Le Fèvre, B., Pin, C., 2005. A straightforward separation scheme for concomitant Lu-Hf and Sm-Nd isotope ratio and isotope dilution analysis. Anal. Chim. Acta 543, 209–221.
29. Li, C.-F., Chen, F., Li, X.-H., 2007. Precise isotopic measurements of sub-nanogram Nd of standard reference material by thermal ionization mass spectrometry using NdO^+ technique. Int. J. Mass Spectrom. 266, 34–41.
30. Li, C.-F., et al., 2011a. An evaluation of a single-step extraction chromatography separation method for Sm-Nd isotope analysis of micro-samples of silicate rocks by high-sensitivity thermal ionization mass spectrometry. Anal. Chim. Acta 706, 297–304.
31. Li, C.-F., et al., 2011b. Directly determining $^{143}Nd/^{144}Nd$ isotope ratios using thermal ionization mass spectrometry for geological samples without separation of Sm-Nd. J. Anal. Atom. Spectrom. 26, 2012–2022.
32. Li, C.-F., et al., 2012. Rapid and precise determination of Sr and Nd isotopic ratios in geological samples from the same filament loading by thermal ionization mass spectrometry employing a single-step scheme. Anal. Chim. Acta 727, 54–60.
33. Li, C.-F., et al., 2014. Single-step separation scheme and high-precision isotopic ratios analysis of Sr-Nd-Hf in silicate materials. J. Anal. Atom. Spectrom. 29, 1467–1476.
34. Li, C.-F., et al., 2015. Ce-Nd separation by solid-phase micro-extraction and its application to high-precision $^{142}Nd/^{144}Nd$ measurements using TIMS in geological materials. J. Anal. Atom. Spectrom. 30, 895–902.
35. Luu, T.-H., Hin, R.C., Coath, C.D., Elliott, T., 2019. Bulk chondrite variability in mass independent magnesium isotope compositions – Implications for initial solar system $^{26}Al/^{27}Al$ and the timing of terrestrial accretion. Earth Planet. Sci. Lett. 522, 166–175.
36. Mahlen, N.J., Beard, B.L., Johnson, C.M., Lapen, T.J., 2008. An investigation of dissolution methods for Lu-Hf and Sm-Nd isotope studies in zircon- and garnet-bearing whole-rock samples. Geochem. Geophys. Geosyst. 9, Q01002.
37. Makishima, A., Nath, B.N., Nakamura, E., 2008. New sequential separation procedure for Sr, Nd and Pb isotope ratio measurement in geological material using MC-ICP-MS and TIMS. Geochem. J. 42, 237–246.
38. Mokadem, F., et al., 2015. High-precision radiogenic strontium isotope measurements of the modern and glacial ocean: Limits on glacial-interglacial variations in continental weathering. Earth Planet. Sci. Lett. 415, 111–120.
39. Moynier, F., et al., 2012. Planetary-scale strontium isotopic heterogeneity and the age of volatile depletion of early solar system materials. Astrophys. J. 758,45–52.
40. Mundl, A., et al., 2017. Tungsten-182 heterogeneity in modern ocean island basalts. Science 356, 66–69.
41. Neymark, L.A., Premo, W.R., Mel'nikov, N.N., Emsbo, P., 2014. Precise determination of $\delta^{88}Sr$ in rocks, minerals and waters by double-spike TIMS: a powerful tool in the study of geological, hydrological and biological processes. J. Anal. Atom. Spectrom. 29, 65–75.
42. Peters, B.J., Carlson, R.W., Day, J.M.D., Horan, M.F., 2018. Hadean silicate differentiation preserved by anomalous $^{142}Nd/^{144}Nd$ ratios in the Réunion hotspot source. Nature 555, 89–93.

43. Pin, C., Gannoun, A., Dupont, A., 2014. Rapid, simultaneous separation of Sr, Pb and Nd by extraction chromatography prior to isotope ratios determination by TIMS and MC-ICP-MS. J. Anal. Atom. Spectrom. 29, 1858–1870.
44. Pin, C. and Gannoun, A., 2019a. A triple tandem columns extraction chromatography method for isolation of highly purified neodymium prior to ^{143}Nd/^{144}Nd and ^{142}Nd/^{144}Nd isotope ratios determinations. J. Anal. Atom. Spectrom. 34, 310–318.
45. Pin, C. and Gannoun, A., 2019b. Miniaturized, rapid separation of neodymium from ultramafic and chondritic samples prior to high precision measurements of ^{142,143}Nd/^{144}Nd isotope ratios by TIMS. J. Anal. Atom. Spectrom. 34, 2136–2146.
46. Raczek, I., Jochum, K.P., Hofmann, A.W., 2003. Neodymium and strontium isotope data for USGS reference materials BCR-1, BCR-2, BHVO-1, BHVO-2, AGV-1, AGV-2, GSP-1, GSP-2 and eight MPI-DING reference glasses. Geostandards Newlett. 27, 173–179.
47. Rizo, H., et al., 2016. Preservation of Earth-forming events in the tungsten isotopic composition of modern flood basalts. Science, 2016, 352, 809–812.
48. Roth, A.S.G., et al, 2014. Revisiting the ^{142}Nd deficits in the 1.48 Ga Khariar alkaline rocks, India. Chem. Geol. 386, 238–248.
49. Starr, P.G., et al., 2020. The subduction and exhumation history of the Voltri Ophiolite Italy: Evaluating exhumation mechanisms for high-pressure metamorphic massifs. Lithos 376-377, 105767.
50. Tanaka, T., et al., 2000. JNdi-1: a neodymium isotopic reference in consistency with LaJolla neodymium. Chem. Geol. 168, 279–281.
51. Thirlwall, M.F., 1991. Long-term reproducibility of multicollector Sr and Nd isotope ratio analysis. Chem. Geol. 94, 85–104.
52. Thomsen, E., and Andreasen, R., 2019. Agricultural lime disturbs natural strontium isotope variations: Implications for provenance and migration studies. Sci. Adv. 5, eaav8083.
53. Weis, D., et al., 2006. High-precision isotopic characterization of USGS reference materials by TIMS and MC-ICP-MS. Geochem. Geophys. Geosyst. 7, Q08006.
54. Weisler, M.I., et al., 2016. Cook Island artifact geochemistry demonstrates spatial and temporal extent of pre-European interarchipelago voyaging in East Polynesia. Proc. Natl. Acad. Sci. U. S. A. 113, 8150-8155.
55. White, W.M., 2015. Probing the Earth's Deep Interior through Geochemistry. Geochem. Perspect. 4, number 2, 95–251.
56. Yang, Y.-H., et al., 2010. Combined chemical separation of Lu, Hf, Rb, Sr, Sm and Nd from a single rock digest and precise and accurate isotope determinations of Lu-Hf, Rb-Sr and Sm-Nd isotope systems using Multi-collector ICP-MS and TIMS. Int. J. Mass Spectrom. 290, 120–126.
57. Yang, Y.-H., et al., 2012. Evaluation of Sr chemical purification technique for natural geological samples using common cation-exchange and Sr-specific extraction chromatographic resin prior to MC-ICP-MS or TIMS measurement. J. Anal. Atom. Spectrom. 27, 516–522.
58. Yobregat, E., Fitoussi, C., Bourdon, B., 2017. A new method for TIMS high precision analysis of Ba and Sr isotopes for cosmochemical studies. J. Anal. Atom. Spectrom. 32, 1388–1399.

59. Zhang, W., Hu, Z., 2020. Estimation of isotopic reference values for pure materials and geological reference materials. At. Spectrosc. 41, 93–102.
60. Birck, J.-L. and Allègre, C.J., 1978. Chronology and chemical history of the parent body of basaltic achondrites studied by the ^{87}Rb-^{87}Sr method. Earth Planet. Sci. Lett. 39, 37–51.
61. Chauvel, C., Dupré, B., Jenner, G.A., 1985. The Sm-Nd age of Kambalda volcanics is 500 Ma too old! Earth Planet. Sci. Lett. 74, 315–324.

TABLE 1: Collector configuration used for Sr (a) and Nd (b) isotope measurements on the Nu TIMS during the course of this study. Note that the numbers in bold purple correspond to the mass used for the peak centering for each line. (c) Reverse configuration for Nd used to test if there is any difference between methods b and c.

a.

Sr configuration	H11	H9	H7	H5	H3	H1	L1	L3	Integration time (s)	Quad 1 (V)	Quad 2 (V)
Line 1	**88**	87	86	85	84	83	82	81	16	27	-27
Line 2	89	**88**	87	86	85	84	83	82	16	28	-42
Line 3	90	89	**88**	87	86	85	84	83	16	33	-61
Line 4	91	90	89	**88**	87	86	85	84	16	34	-77
Line 5	92	91	90	89	**88**	87	86	85	16	36	-91

b.

Nd configuration	H11	H10	H9	H8	H7	H6	H5	H4	H3	H2	H1	Ax	L1	L2	L3	L4	Integration time (s)	Quad 1 (V)	Quad 2 (V)
Line 1	155	154	153	152	151	150	149	148	147	146	145	144	143	**142**	141	137	10	-15	127
Line 2	154	153	152	151	150	149	148	147	146	145	144	143	**142**	141	140	136	10	-15	134
Line 3	153	152	151	150	149	148	147	146	145	144	143	**142**	141	140	139	135	10	-17	139
Line 4	152	151	150	149	148	147	146	145	144	143	**142**	141	140	139	138	134	10	-17	145
Line 5	151	150	149	148	147	146	145	144	143	**142**	141	140	139	138	137	133	10	-17	148

c.

Nd Reverse	H11	H10	H9	H8	H7	H6	H5	H4	H3	H2	H1	Ax	L1	L2	L3	L4	Integration time (s)	Quad 1 (V)	Quad 2 (V)
Line 1	151	150	149	148	147	146	145	144	143	**142**	141	140	139	138	137	133	10	-18	149
Line 2	152	151	150	149	148	147	146	145	144	143	**142**	141	140	139	138	134	10	-18	146
Line 3	153	152	151	150	149	148	147	146	145	144	143	**142**	141	140	139	135	10	-18	140
Line 4	154	153	152	151	150	149	148	147	146	145	144	143	**142**	141	140	136	10	-17	137
Line 5	155	154	153	152	151	150	149	148	147	146	145	144	143	**142**	141	137	10	-17	131

TABLE 2: a. Potential interferences (a) in the mass region 84-88 affecting the Sr isotope results and (b) in the mass region 142-150 affecting the Nd isotope results. In practice, Kr, oxides and doubly charged ions constitute a major issue when using plasma source mass spectrometers, but they are very rare when using a TIMS. Only interferences coming from Rb and Ce-Sm (bold purple) are considered when measuring Sr and Nd isotopes on a TIMS. A good Sr and Nd chemical separation prior to isotope analyses on the TIMS is mandatory.

a.

Sr	^{84}Sr$^+$	^{86}Sr$^+$	^{87}Sr$^+$	^{88}Sr$^+$
Kr	^{84}Kr$^+$	^{86}Kr$^+$		
Rb			**^{87}Rb$^+$**	
REE	^{168}Yb^{2+}	^{172}Yb^{2+}	^{174}Yb^{2+}	^{176}Yb^{2+}
	^{168}Er^{2+}			
				^{176}Lu^{2+}
			^{174}Hf^{2+}	^{176}Hf^{2+}
Fe oxides		^{54}Fe^{16}O$_2^+$	^{54}Fe^{16}O^{17}O$^+$	^{54}Fe^{16}O^{18}O$^+$
				^{54}Fe^{17}O$_2^+$
				^{56}Fe^{16}O$_2^+$
Zn oxides	^{68}Zn^{16}O$^+$	^{68}Zn^{18}O$^+$		
		^{70}Zn^{16}O$^+$	^{70}Zn^{17}O$^+$	^{70}Zn^{18}O$^+$
Ga oxides		^{69}Ga^{17}O$^+$	^{69}Ga^{18}O$^+$	
			^{71}Ga^{16}O$^+$	^{71}Ga^{17}O$^+$
Ca dimers	^{40}Ca^{44}Ca$^+$	^{40}Ca^{46}Ca$^+$		^{40}Ca^{48}Ca$^+$
	^{42}Ca$_2^+$	^{42}Ca^{44}Ca$^+$		^{42}Ca^{46}Ca$^+$
		^{43}Ca$_2^+$	^{43}Ca^{44}Ca$^+$	
				^{44}Ca$_2^+$

b.

Nd	^{142}Nd	^{143}Nd	^{144}Nd	^{145}Nd	^{146}Nd	^{148}Nd	^{150}Nd
Ce	**^{142}Ce$^+$**						
Sm			**^{144}Sm$^+$**			**^{148}Sm$^+$**	**^{150}Sm+**
Ba oxides					^{130}Ba^{16}O	^{132}Ba^{16}O	^{134}Ba^{16}O
							^{132}Ba^{18}O
Ru oxides			^{96}Ru^{16}O$_3^+$		^{98}Ru^{16}O$_3^+$	^{100}Ru^{16}O$_3^+$	^{102}Ru^{16}O$_3^+$

TABLE 3: Strontium and neodymium isotope compositions for pure standard solutions and terrestrial rocks measured in the course of this study. All the ratios are multidynamic except the ^{84}Sr/^{86}Sr which are multistatic. Rep = the solution was loaded a second time on a different filament.

		^{87}Sr/^{86}Sr	**2se/2sd**	**^{84}Sr/^{86}Sr**	**2se/2sd**	**Yield (%)**	**^{143}Nd/^{144}Nd**	**2se/2sd**	**^{145}Nd/^{144}Nd**	**2se/2sd**	**^{148}Nd/^{144}Nd**	**2se/2sd**	**^{150}Nd/^{144}Nd**	**2se/2sd**	**Yield (%)**
Pure standard Solutions	NBS 987	0.7102467	4.3×10^{-6} (n = 38)	0.0564902	1.8×10^{-6} (n=38)										
	Rennes-Ames						0.5119537	2.2×10^{-6} (n=31)	0.3484004	1.3×10^{-6} (n=31)	0.2415798	1.9×10^{-6} (n=31)	0.2364508	5.6×10^{-6} (n=31)	
Terrestrial rocks															
BHVO-2	BHVO-2 a						0.5129680	7.3×10^{-7}	0.3484000	2.2×10^{-7}	0.2415805	3.3×10^{-7}	0.2364501	5.3×10^{-7}	34
	BHVO-2 Pam	0.7034753	1.9×10^{-6}	0.0564891	5.1×10^{-7}	29	0.5129658	6.2×10^{-7}	0.3483998	1.8×10^{-7}	0.2415793	2.6×10^{-7}	0.2364491	4.5×10^{-7}	40
	BHVO-2 b	0.7034737	1.2×10^{-6}	0.0564890	4.5×10^{-7}	86	0.5129653	6.5×10^{-7}	0.3483992	2.1×10^{-7}	0.2415791	2.7×10^{-7}	0.2364487	4.0×10^{-7}	84
	BHVO-2 c	0.7034765	1.4×10^{-6}	0.0564899	5.3×10^{-7}	75	0.5129656	6.0×10^{-7}	0.3483997	1.7×10^{-7}	0.2415802	2.5×10^{-7}	0.2364502	3.6×10^{-7}	89
	BHVO-2 c rep	0.7034746	1.4×10^{-6}	0.0564883	4.4×10^{-7}										
	mean	**0.7034750**	**2.3×10^{-6}**	**0.0564891**	**1.3×10^{-6}**		**0.5129662**	**2.5×10^{-6}**	**0.3483996**	**7.2×10^{-7}**	**0.2415798**	**1.4×10^{-6}**	**0.2364495**	**1.5×10^{-6}**	
BCR-2	BCR-2 a	0.7050090	1.5×10^{-6}	0.0564898	5.1×10^{-7}	27	0.5126183	8.5×10^{-7}	0.3484002	2.9×10^{-7}	0.2415858	3.7×10^{-7}	0.2364560	5.8×10^{-7}	18
	BCR-2 b	0.7050103	9.9×10^{-7}	0.0564873	4.5×10^{-7}	78									
	BCR-2 c	0.7050093	1.3×10^{-6}	0.0564893	4.3×10^{-7}	93	0.5126142	5.1×10^{-7}	0.3483987	1.4×10^{-7}	0.2415789	1.9×10^{-7}	0.2364471	2.9×10^{-7}	90
	BCR-2 c rep	0.7050077	1.1×10^{-6}	0.0564889	4.3×10^{-7}										
	mean	**0.7050091**	**2.2×10^{-6}**	**0.0564893**	**8.4×10^{-7}**		**0.5126162**	**5.7×10^{-6}**	**0.3483994**	**2.1×10^{-6}**	**0.2415824**	**9.7×10^{-6}**	**0.2364515**	**1.3×10^{-5}**	
BR-24	BR-24 a	0.7050381	1.2×10^{-6}	0.0564882	4.2×10^{-7}	87	0.5127711	5.5×10^{-7}	0.3483991	1.5×10^{-7}	0.2415791	2.3×10^{-7}	0.2364482	3.9×10^{-7}	92
	BR-24 b	0.7050380	1.6×10^{-6}	0.0564881	5.9×10^{-7}	87	0.5127711	5.3×10^{-7}	0.3483988	1.7×10^{-7}	0.2415796	2.3×10^{-7}	0.2364496	3.5×10^{-7}	89
	BR-24 b rep	0.7050379	1.2×10^{-6}	0.0564878	4.1×10^{-7}										
	mean	**0.7050380**	**1.8×10^{-7}**	**0.0564880**	**4.2×10^{-7}**		**0.5127711**	**2.8×10^{-8}**	**0.3483989**	**4.7×10^{-7}**	**0.2415793**	**7.9×10^{-7}**	**0.2364489**	**2.1×10^{-6}**	
BIR-1	BIR-1 a	0.7031000	1.5×10^{-6}	0.0564888	4.7×10^{-7}	74	0.5130710	9.2×10^{-7}	0.3483992	2.7×10^{-7}	0.2415824	4.1×10^{-7}	0.2364516	5.5×10^{-7}	87
	BIR-1 b	0.7030985	1.6×10^{-6}	0.0564892	5.6×10^{-7}	71	0.5130734	9.5×10^{-7}	0.3483992	2.6×10^{-7}	0.2415795	3.6×10^{-7}	0.2364482	5.9×10^{-7}	86
	BIR-1 b rep	0.7030959	1.3×10^{-6}	0.0564898	4.2×10^{-7}										
	mean	**0.7030981**	**4.1×10^{-6}**	**0.0564893**	**1.1×10^{-6}**		**0.5130722**	**3.5×10^{-6}**	**0.3483992**	**5.7×10^{-8}**	**0.2415810**	**4.0×10^{-6}**	**0.2364499**	**4.8×10^{-6}**	
Be-N	Be-N a	0.7038004	1.6×10^{-6}	0.0564873	6.0×10^{-7}	75	0.5128642	6.0×10^{-7}	0.3483994	1.8×10^{-7}	0.2415804	2.3×10^{-7}	0.2364517	3.9×10^{-7}	91
	Be-N a rep	0.7037995	1.1×10^{-6}	0.0564875	4.4×10^{-7}										
	Be-N b	0.7037999	1.5×10^{-6}	0.0564883	5.1×10^{-7}	89	0.5128617	6.1×10^{-7}	0.3483991	1.8×10^{-7}	0.2415815	2.3×10^{-7}	0.2364530	3.6×10^{-7}	86
	mean	**0.7037999**	**8.6×10^{-7}**	**0.0564877**	**1.1×10^{-6}**		**0.5128629**	**3.5×10^{-6}**	**0.3483993**	**4.5×10^{-7}**	**0.2415809**	**1.6×10^{-6}**	**0.2364524**	**1.8×10^{-6}**	
RGM-1	RGM1-a					12									9
	RGM-1 b	0.7042043	1.4×10^{-6}	0.0564873	4.4×10^{-7}	71	0.5127778	6.9×10^{-7}	0.3483999	2.1×10^{-7}	0.2415802	2.6×10^{-7}	0.2364489	4.1×10^{-7}	91
	RGM-1 b rep	0.7041943	1.1×10^{-6}	0.0564886	4.1×10^{-7}										
	RGM-1 c					85									
	mean	**0.7041993**	**1.4×10^{-5}**	**0.0564880**	**1.9×10^{-6}**										
AGV-2	AGV-2 a	0.7039781	1.8×10^{-6}	0.0564908	6.1×10^{-7}	14	0.5127720	9.0×10^{-7}	0.3484012	3.3×10^{-7}	0.2415795	3.5×10^{-7}	0.2364480	6.7×10^{-7}	15
	AGV-2 b	0.7039843	9.5×10^{-7}	0.0564875	3.9×10^{-7}	85	0.5127688	6.2×10^{-7}	0.3483987	2.0×10^{-7}	0.2415780	2.6×10^{-7}	0.2364465	4.1×10^{-7}	79
	AGV-2 c	0.7039800	1.2×10^{-6}	0.0564896	4.5×10^{-7}	93	0.5127698	5.4×10^{-7}	0.3483988	1.5×10^{-7}	0.2415810	2.3×10^{-7}	0.2364508	3.6×10^{-7}	91
	AGV-2 c rep	0.7039835	1.3×10^{-6}	0.0564877	4.4×10^{-7}										
	mean	**0.7039814**	**5.9×10^{-6}**	**0.0564889**	**3.2×10^{-6}**		**0.5127702**	**3.3×10^{-6}**	**0.3483996**	**2.8×10^{-6}**	**0.2415795**	**3.0×10^{-6}**	**0.2364485**	**4.4×10^{-6}**	

TABLE 4: Comparison between $(^{87}\text{Sr}/^{86}\text{Sr})_{\text{multidyn}}$ when using the time drift correction, or not.

	With time drift correction		Without time drift correction		Relative difference (ppm)	n
	^{87}Sr/^{86}Sr	2sd	^{87}Sr/^{86}Sr	2sd		
NBS 987	0.7102466	4.1×10^{-6}	0.7102490	5.0×10^{-6}	3.4	37
BHVO-2	0.7034750	2.3×10^{-6}	0.7034779	2.6×10^{-6}	4.0	4
BCR-2	0.7050091	2.2×10^{-6}	0.7050112	2.8×10^{-6}	3.0	4
BR-24	0.7050380	1.8×10^{-7}	0.7050403	1.0×10^{-6}	3.2	3
BIR-1	0.7030981	4.1×10^{-6}	0.7031002	5.1×10^{-6}	3.0	3
Be-N	0.7037999	8.6×10^{-7}	0.7038028	2.0×10^{-6}	4.1	3
AGV-2	0.7039814	5.9×10^{-6}	0.7039841	5.7×10^{-6}	3.7	4

FIGURE 1: a. Schematic showing where the zoom lens system allowing peak alignment while having fixed Faraday detectors sits on the Nu TIMS, and what happens to the ion beams when using or not the zoom lens system. a-1: No voltage is applied on quads 1 and 2, resulting in two ion beams diverging and being unfocused at the collector array. a-2: A voltage is applied on quad 1 only, resulting in two ion beams being focused but the natural dispersion of these ion beams does not align with the collector array. a-3: Voltages are now applied on both quads 1 and 2, resulting in two ion beams being now focused at the correct collectors.

b. Peak alignment achieved with fixed Faraday detectors for Sr and Nd isotopes when applying adequate voltages on the zoom lens system. The isotopes ^{84}Sr, ^{86}Sr, ^{87}Sr and ^{88}Sr are collected in H1, H5, H7 and H9 detectors, respectively (C-1). The isotopes ^{142}Nd, ^{143}Nd, ^{144}Nd, ^{145}Nd, ^{146}Nd, ^{148}Nd and ^{150}Nd are collected in L2, L1, Ax, H1, H2, H4 and H6, respectively (C-2).

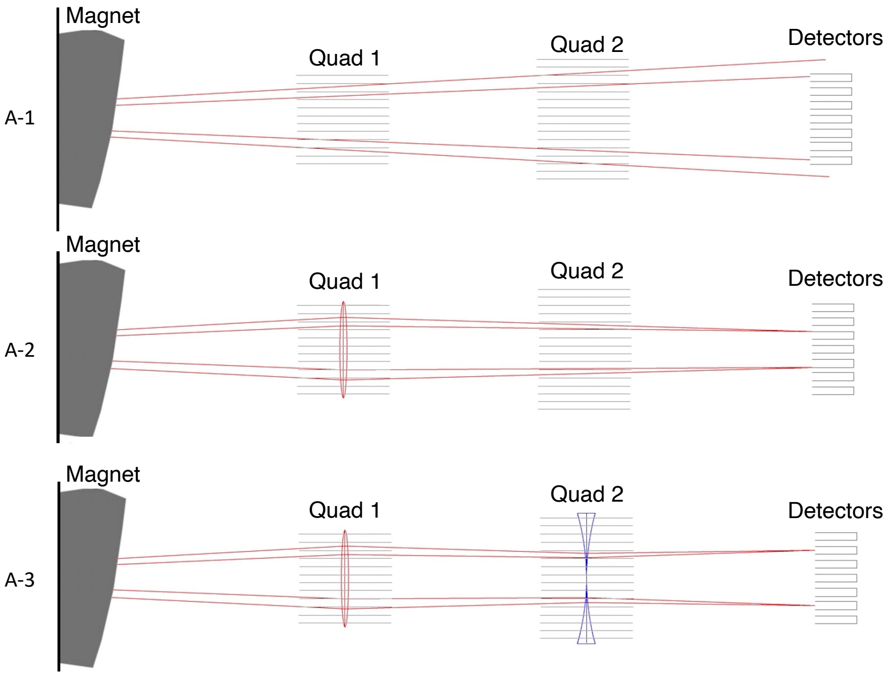

A.

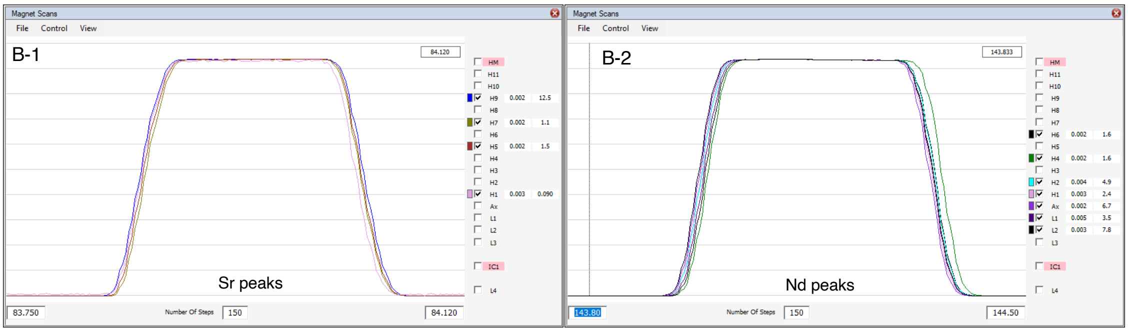

B-1: 84.120

☐ HM
☐ H11
☐ H10
☑ H9 0.002 12.5
☐ H8
☑ H7 0.002 1.1
☐ H6
☑ H5 0.002 1.5
☐ H4
☐ H3
☐ H2
☑ H1 0.003 0.090
☐ Ax
☐ L1
☐ L2
☐ L3
☐ IC1
☐ L4

83.750 Number Of Steps 150 84.120

B-2: 143.833

☐ HM
☐ H11
☐ H10
☐ H9
☐ H8
☐ H7
☑ H6 0.002 1.6
☐ H5
☑ H4 0.002 1.6
☐ H3
☑ H2 0.004 4.9
☑ H1 0.003 2.4
☑ Ax 0.002 6.7
☑ L1 0.005 3.5
☑ L2 0.003 7.8
☐ L3
☐ IC1
☐ L4

143.80 Number Of Steps 150 144.50

B.

FIGURE 2: Comparison between the internal errors typically obtained when running the Sr isotope analyses (i) with more than 10V of signal on $^{88}Sr^{+}$ for 6-7 hours (i.e. our standard conditions, blue dots) and (ii) with more than 10V of signal on $^{88}Sr^{+}$ for 2 hours only (orange crosses). An estimation of the internal errors obtained when running with less than 3V of signal for 2 hours is also shown for comparison (black arrow).

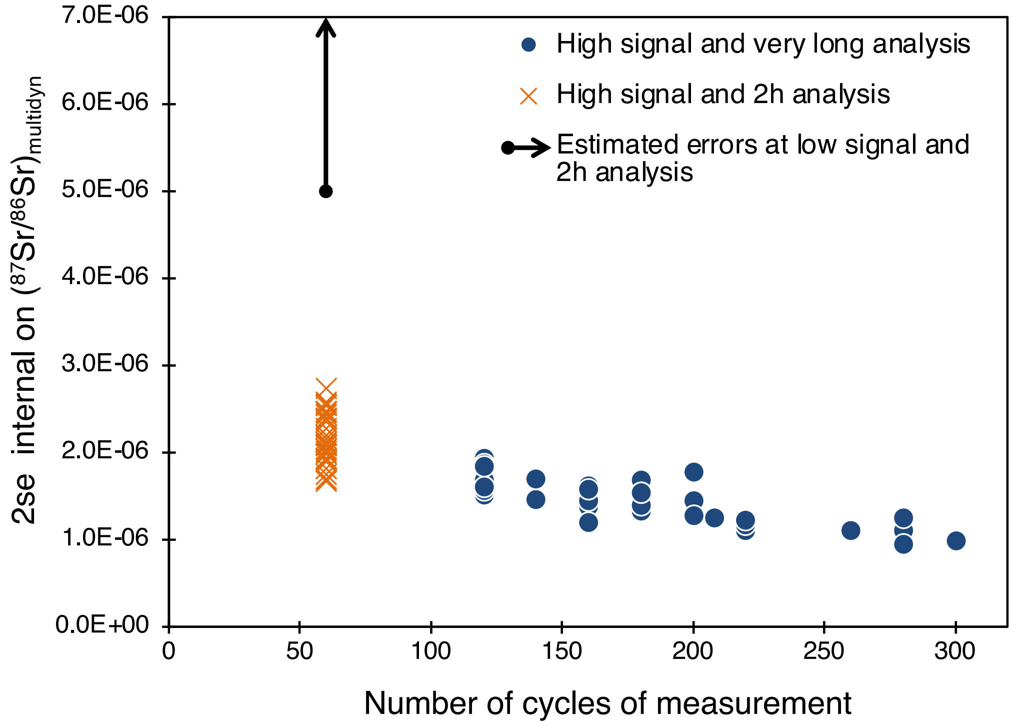

FIGURE 3:

a. Comparison of our mean $(^{87}Sr/^{86}Sr)_{multidyn}$ (blue circle) with literature data (grey circles) for the pure Sr standard solution NBS 987. Note that the yellow circle corresponds to the recommended value reported by Zhang and Hu (2020) after a compilation of the data available in Georem. Error bars correspond to 2 sd. Literature: (a) Raczek et al. 2003, (b) Weis et al. 2006, (c) Makishima et al. 2008, (d) Aciego et al. 2009, (e) Yang et al. 2010, (f) Chauvel et al. 2011, (g) Yang et al. 2012, (h) Carpentier et al. 2014, (i) Li et al. 2014, (j) Pin et al. 2014, (k) Mokadem et al. 2015, (l) Fourny et al. 2016, (m) Yobregat et al. 2017, (n) Di et al. 2021, (o) Zhang and Hu 2020.

b. Comparison between $(^{87}Sr/^{86}Sr)_{multidyn}$ and $(^{87}Sr/^{86}Sr)_{multistat}$ measured in the NBS 987 standard solution over a period of ~ 10 months on the Nu TIMS. Error bars on individual data correspond to internal 2 se.

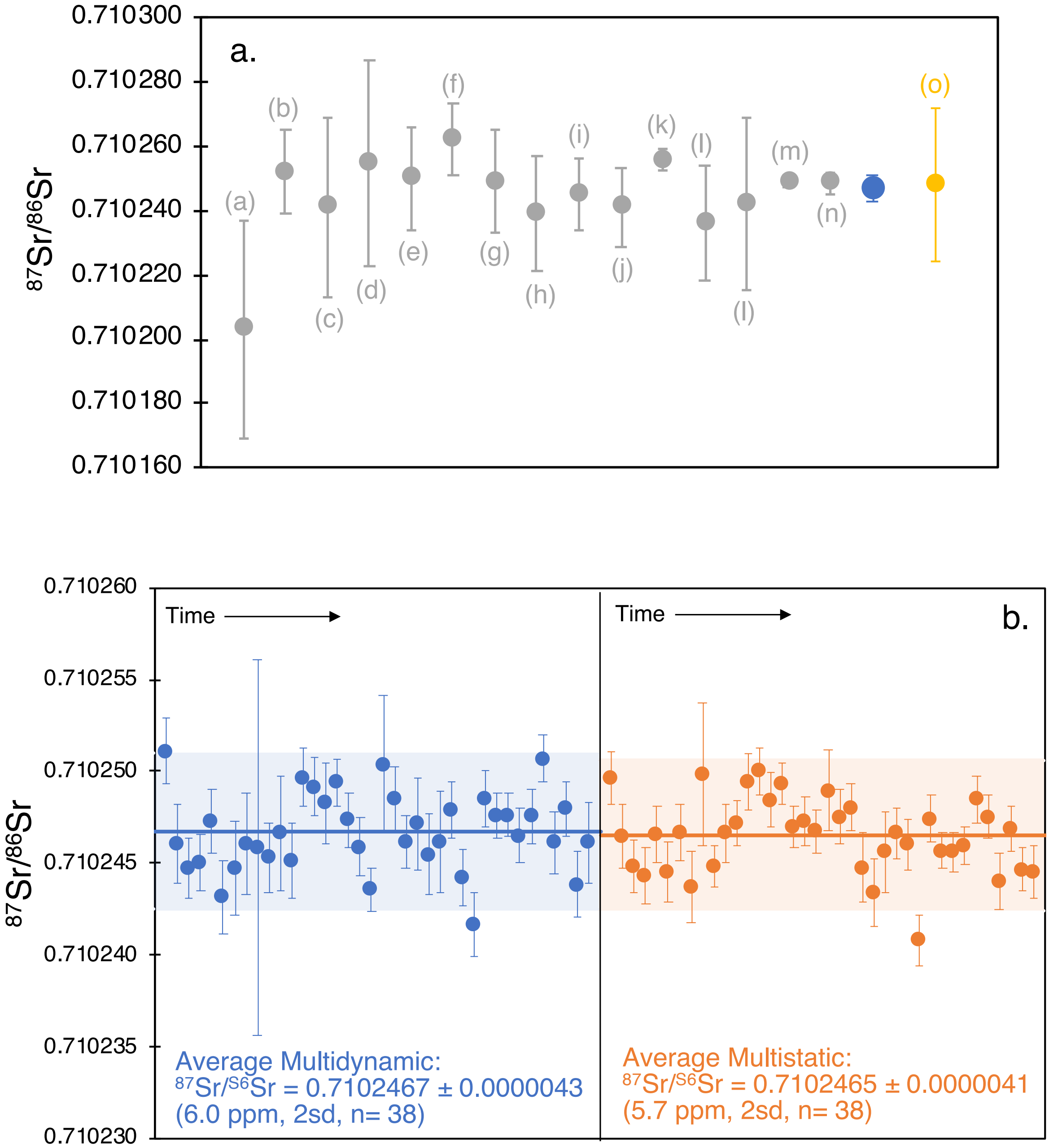

FIGURE 4:

a. Comparison of our mean $(^{143}Nd/^{144}Nd)_{multidyn}$ measured for the pure Nd standard solutions JNDi-1 and Rennes-Ames (blue circles) with literature data (grey circles). Note that we added the reference Fourny et al. (2016) for comparison, given the few data available in the literature for the Nd standard solution Rennes-Ames. Note that the yellow circle corresponds to the recommended value reported by Zhang and Hu (2020) after a compilation of the data available in Georem. Error bars correspond to 2 s.d. Literature: (a) Tanaka et al. 2000, (b) Le Fèvre and Pin 2005, (c) Li et al. 2007, (d) Aciego et al. 2009, (e) Chu et al. 2009, (f) Li et al 2011a, (g) Li et al 2011b, (h) Ali and Srinivasan 2011, (i) Li et al. 2014, (j) Pin et al. 2014, (k) Fourny et al. 2016, (l) Garçon et al. 2018, (m) Pin and Gannoun 2019a, (n) Pin and Gannoun 2019b, (o) Zhang and Hu 2020, (p) Chauvel and Blichert-Toft 2001, (q) Caro et al. 2003, (r) Caro et al. 2006, (s) Weis et al. 2006, (t) Chauvel et al. 2011.

b. Comparison between $(^{143}Nd/^{144}Nd)_{multidyn}$ and $(^{143}Nd/^{144}Nd)_{multistat}$ measured in Rennes-Ames over a period of ~ 8 months on the Nu TIMS. Error bars on individual data correspond to internal 2 se.

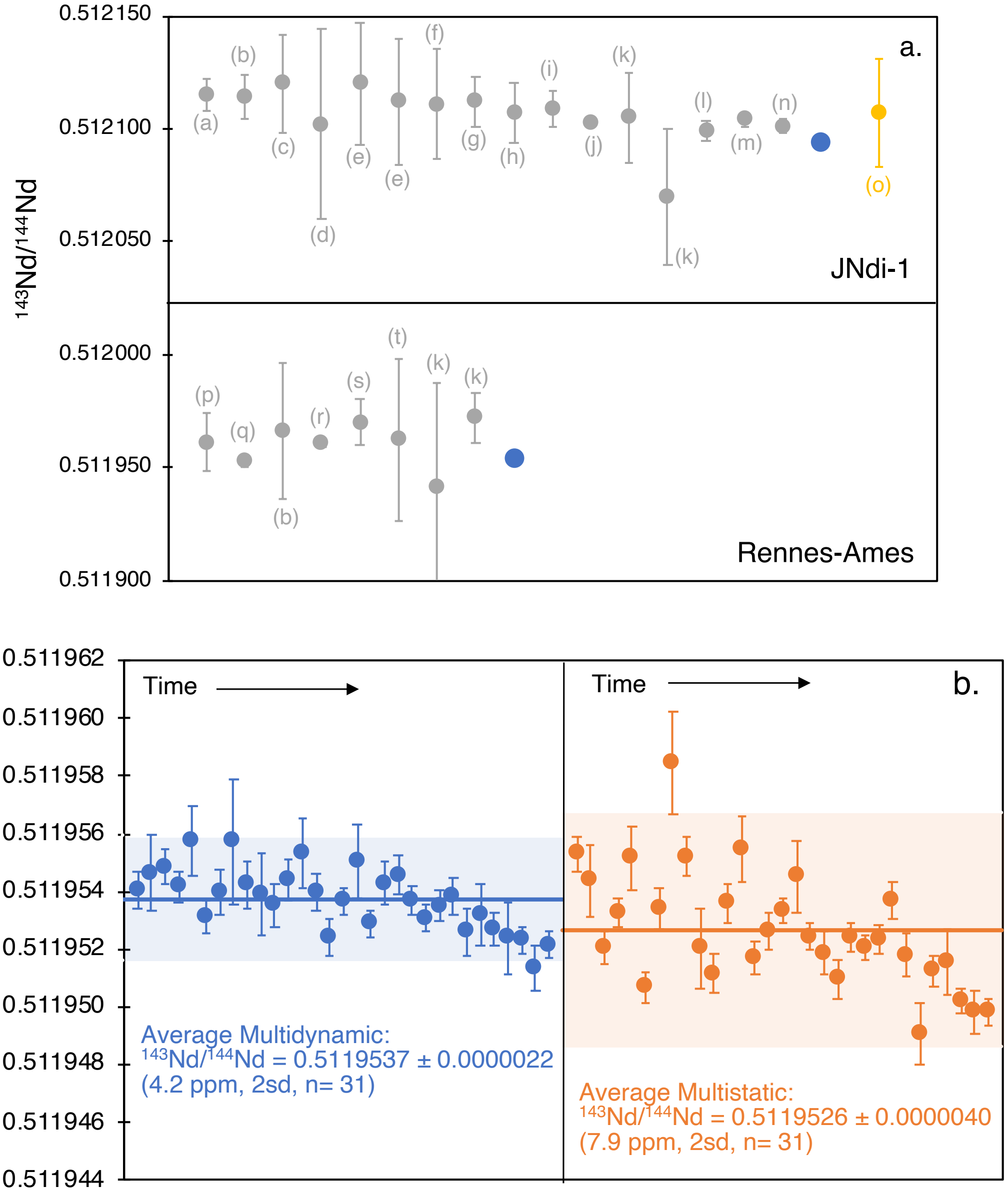

FIGURE 5:

Stable Sr and Nd isotope compositions of the pure standard solutions NBS 987 (a) and Rennes-Ames (b-c) obtained in the course of this study. Error bars correspond to 2 s.e. For comparison are also plotted the latest high precision data (mean ± 2 s.d.) from Burckhardt et al. (2019) and Pin and Gannoun (2019).

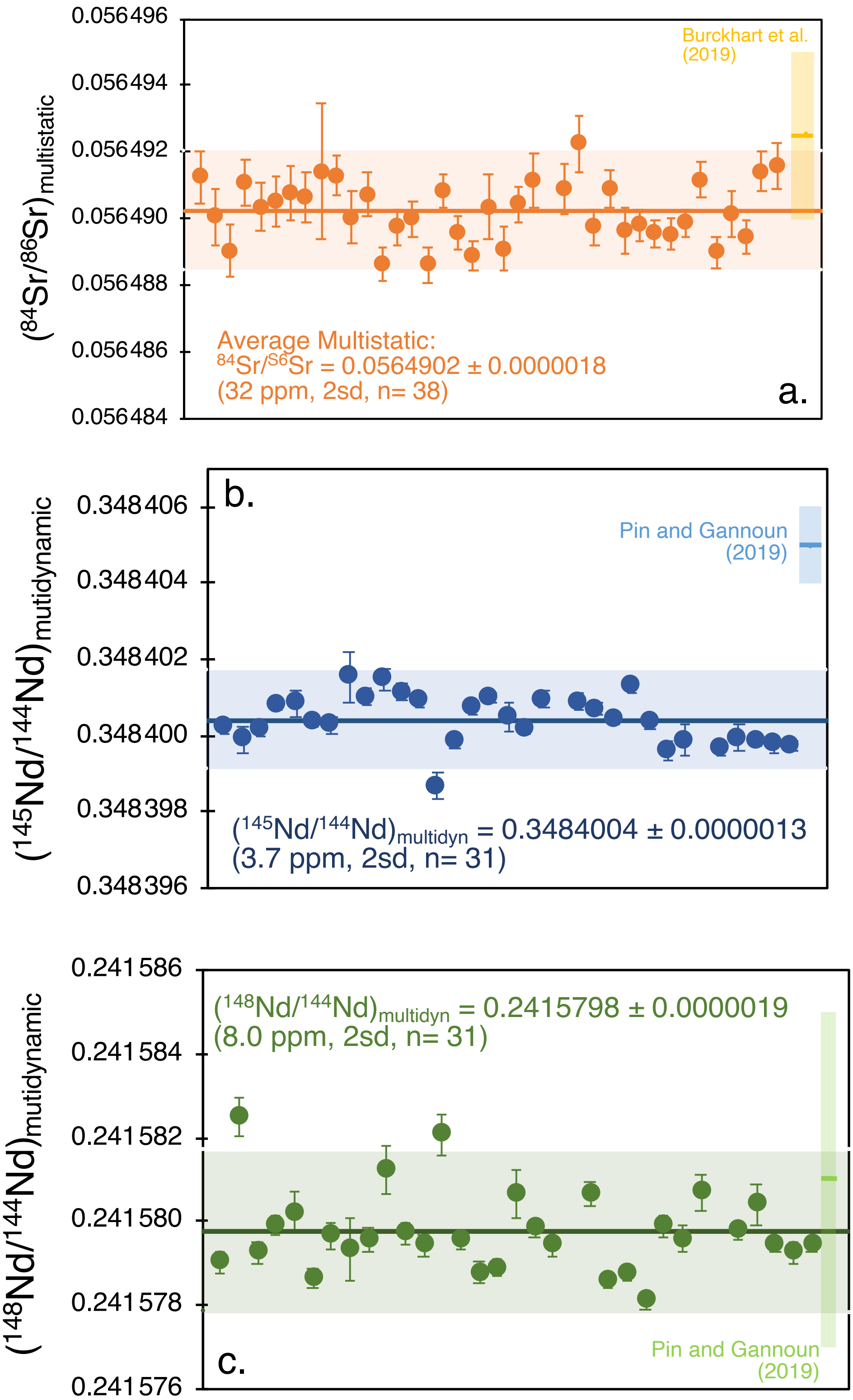

FIGURE 6:

Comparison between the theoretical precision modelled on multidynamic $^{87}Sr/^{86}Sr$ (blue line) and the actual uncertainties obtained for our analyses of NBS 987 (purple diamonds) and geostandards (green dots), with time drift correction (a) and without time drift correction (b).

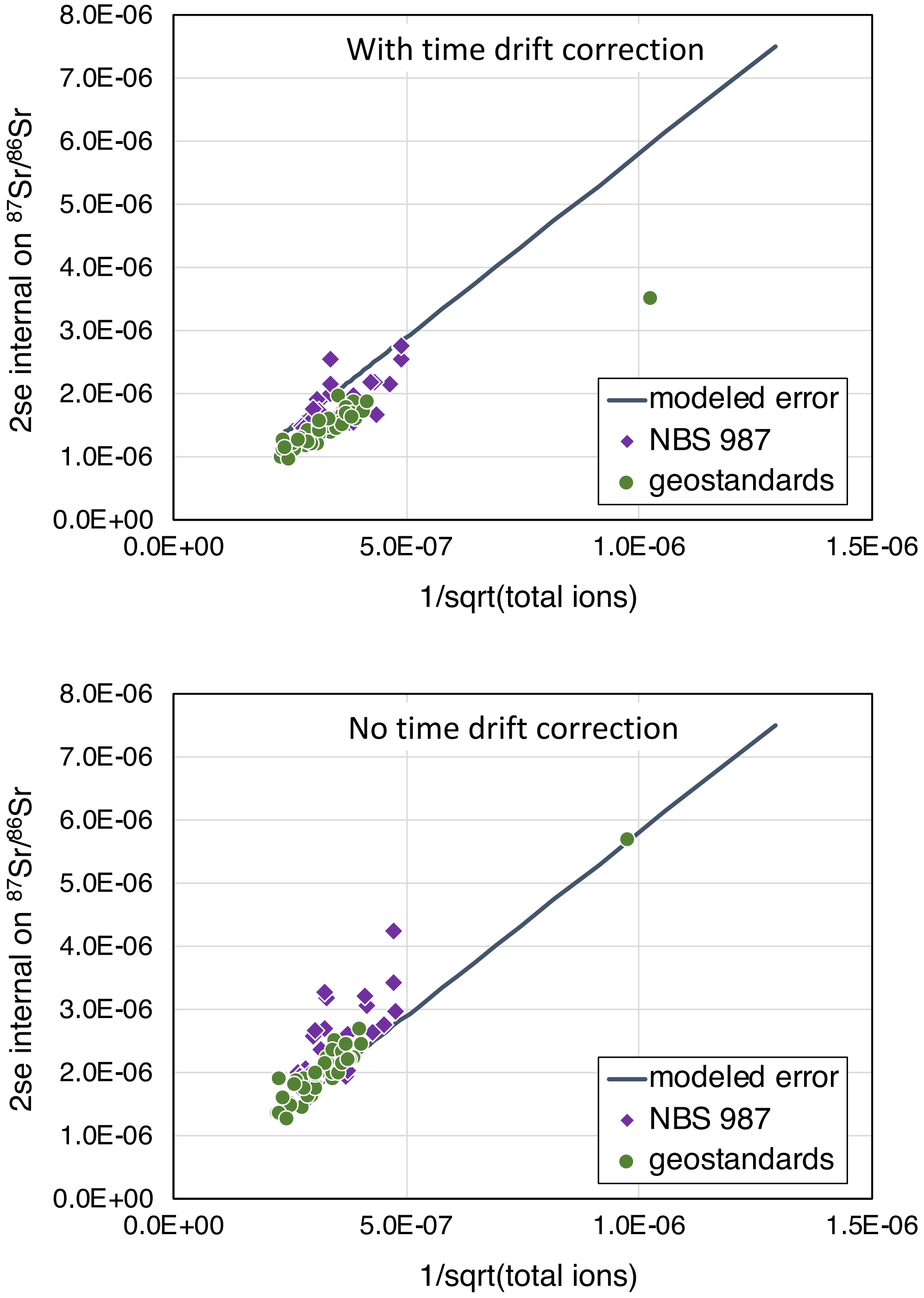

A.

B.

FIGURE 7:

Multidynamic $^{87}Sr/^{86}Sr$ measured for different geostandards in the course of this study (blue symbols) and comparison with literature data (grey symbols). BCR-1, BHVO-1, BIR-1 and AGV-1 are represented as circles, while BCR-2, BHVO-2 and AGV-2 are represented as diamonds. Note that the data from Raczek et al. (2003) have been renormalized to 0.710248 given the different $^{87}Sr/^{86}Sr$ they reported for NBS 987 compared to other studies (see Figure 3a). Recommended values from Zhang and Hu (2020) are also shown for comparison (yellow symbols). Literature: (a-o) same as in figure 3a. (p) Li et al. 2012, (q) Neymark et al. 2014, (r) Klaver et al. 2015, (s) Jweda et al. 2016, (t) Fourny et al. 2019, (u) Koornneef et. 2015.

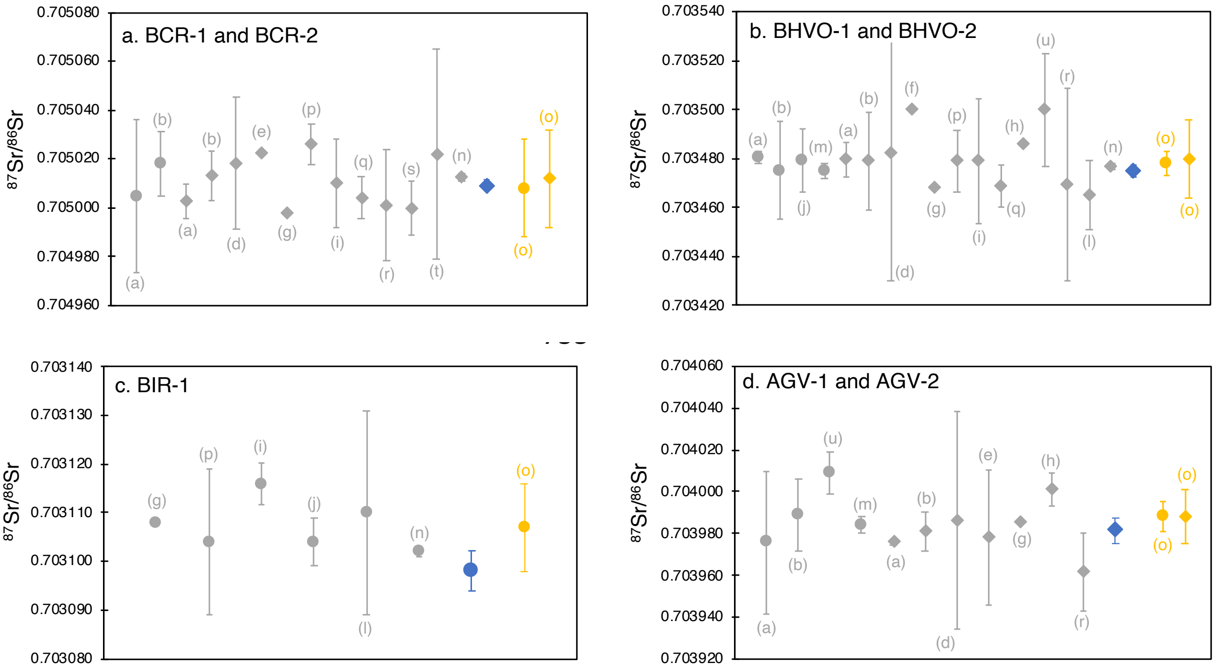

FIGURE 8:

Multidynamic $^{143}Nd/^{144}Nd$ measured for different geostandards in the course of this study (blue symbols) and comparison with the literature. BCR-1, BHVO-1, BIR-1 and AGV-1 are represented as circles, while BCR-2, BHVO-2 and AGV-2 are represented as diamonds. Recommended values from Zhang and Hu (2020) are also shown for comparison (yellow symbols). Literature: (a-t) same as in Figure 4a, (u) Raczek et al. 2003, (v) Mahlen et al. 2008, (w) Yang et al. 2010, (x) Li et al. 2012, (y) Klaver et al. 2015, (z) Li et al. 2015, (aa) Carpentier et al. 2014, (ab) Koornneef et al. 2015.

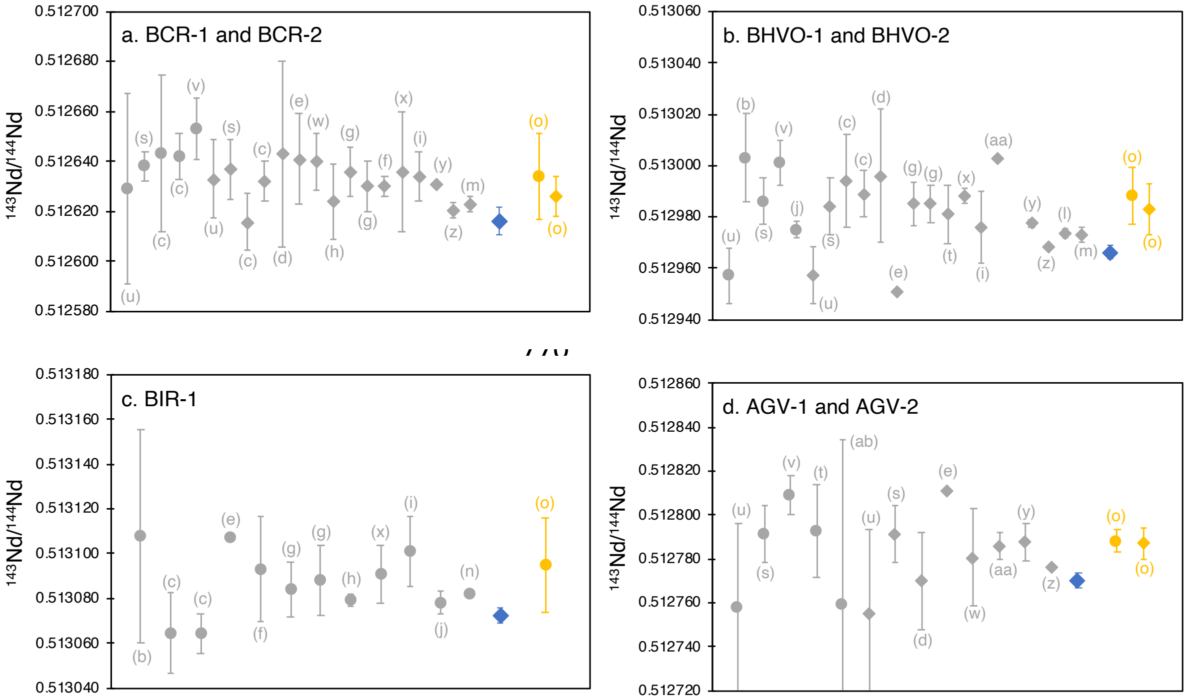

FIGURE 9:

a. Improvement on the uncertainty of the age determined from a Rb-Sr isochron with improvement of the precision on the $^{87}Sr/^{86}Sr$ for extraterrestrial materials (here for ~ 4.55 Ga old eucrites, Birck et al. 1978). We assumed an error of 1% on $^{87}Rb/^{86}Sr$ as stated in Birck et al. (1978).

b. Improvement on the uncertainty of the age determined from a Sm-Nd isochron with improvement of the precision on the $^{143}Nd/^{144}Nd$ for terrestrial materials (here for 2.76 Ga old samples from Kambalda, Chauvel et al. 1985). We assumed an error of 0.2% on the $^{147}Sm/^{144}Nd$ as estimated in Chauvel et al. (1985).

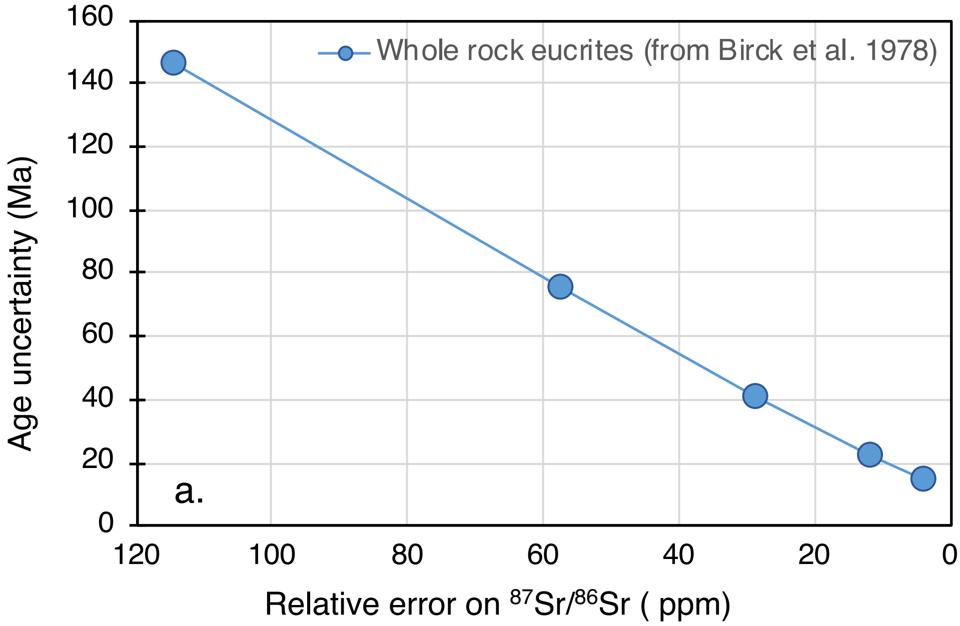

A.

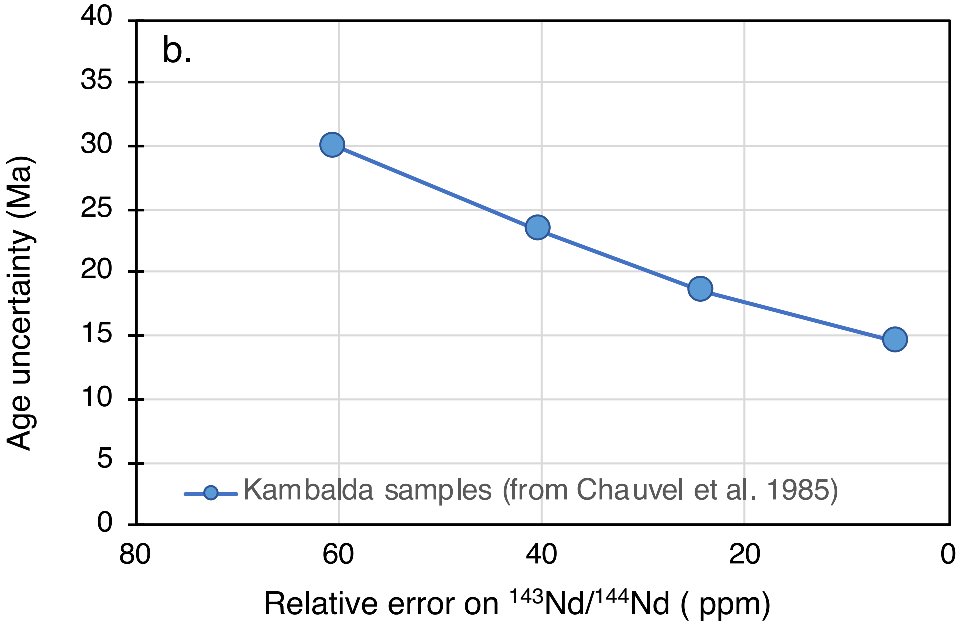

B.